Monthly Notices
of the
ROYAL ASTRONOMICAL SOCIETY

MNRAS **493,** 6033–6049 (2020)
Advance Access publication 2020 March 9

doi:10.1093/mnras/staa631

The MAVERIC survey: a hidden pulsar and a black hole candidate in ATCA radio imaging of the globular cluster NGC 6397

Yue Zhao [1]★ Craig O. Heinke [1] Vlad Tudor [2] Arash Bahramian [2] James C. A. Miller-Jones [2] Gregory R. Sivakoff,[1] Jay Strader,[3] Laura Chomiuk,[3] Laura Shishkovsky,[3] Thomas J. Maccarone,[4] Manuel Pichardo Marcano[4] and Joseph D. Gelfand[5,6]

[1]*Department of Physics, University of Alberta, CCIS 4-183, Edmonton, AB T6G 2E1, Canada*
[2]*International Centre for Radio Astronomy Research, Curtin University, GPO Box U1987, Perth, WA 6845, Australia*
[3]*Department of Physics and Astronomy, Michigan State University, East Lansing, MI 48824, USA*
[4]*Department of Physics, Texas Tech University, Box 41051, Lubbock, TX 79409-1051, USA*
[5]*New York University Abu Dhabi, P.O. Box 129188, Abu Dhabi, United Arab Emirates*
[6]*NYU Center for Cosmology and Particle Physics, New York, NY 10003, USA*

Accepted 2020 February 25. Received 2020 January 3; in original form 2020 January 3

ABSTRACT

Using a 16.2-h radio observation by the Australia Telescope Compact Array and archival *Chandra* data, we found $>5\sigma$ radio counterparts to four known and three new X-ray sources within the half-light radius ($r_{\rm h}$) of the Galactic globular cluster NGC 6397. The previously suggested millisecond pulsar (MSP) candidate, U18, is a steep-spectrum ($S_\nu \propto \nu^\alpha$; $\alpha = -2.0^{+0.4}_{-0.5}$) radio source with a 5.5-GHz flux density of 54.7 ± 4.3 μJy. We argue that U18 is most likely a 'hidden' MSP that is continuously hidden by plasma shocked at the collision between the winds from the pulsar and companion star. The non-detection of radio pulsations so far is probably the result of enhanced scattering in this shocked wind. On the other hand, we observed the 5.5-GHz flux of the known MSP PSR J1740−5340 (U12) to decrease by a factor of >2.8 during epochs of 1.4-GHz eclipse, indicating that the radio flux is absorbed in its shocked wind. If U18 is indeed a pulsar whose pulsations are scattered, we note the contrast with U12's flux decreases in eclipse, which argues for two different eclipse mechanisms at the same radio frequency. In addition to U12 and U18, we also found radio associations for five other *Chandra* X-ray sources, four of which are likely background galaxies. The last, U97, which shows strong Hα variability, is mysterious; it may be either a quiescent black hole low-mass X-ray binary or something more unusual.

Key words: stars: neutron – pulsars: general – globular clusters: general – globular clusters: individual (NGC 6397) – X-rays: binaries.

1 INTRODUCTION

X-ray observations have revealed that Galactic globular clusters (GCs) host an overabundance of X-ray sources, which are thought to originate from compact binaries formed through close encounters in the dense cluster cores (Fabian, Pringle & Rees 1975; Hills 1976; Bailyn, Grindlay & Garcia 1990; Camilo & Rasio 2005; Ivanova et al. 2006). One class of dynamically formed close binaries consists of low-mass X-ray binaries (LMXBs), where neutron stars (NSs) accrete matter from low-mass companion stars (Lewin & Joss 1983; Grindlay et al. 1984). These LMXBs are the progenitors of millisecond pulsars (MSPs), radio pulsars with very stable (low $\dot{P}$) millisecond-scale spin periods ($P \sim 1$–10 ms) and low spin-down inferred dipole magnetic fields ($B \sim 10^8$–10^9 G) (Manchester 2017), which are also abundant in GCs (e.g. Camilo & Rasio 2005). Cataclysmic variables (CVs), white dwarfs (WDs) accreting from low-mass stars, can also be produced dynamically in dense GCs (Heinke et al. 2003; Pooley et al. 2003; Ivanova et al. 2006; Pooley & Hut 2006), but in many clusters most CVs are primordial in origin (Verbunt & Meylan 1988; Davies 1997; Kong et al. 2006; Bassa et al. 2008; Haggard, Cool & Davies 2009; Cheng et al. 2018; Belloni et al. 2019). Chromospherically active binaries (ABs), which are close binaries involving rapidly rotating late (K–M)-type

★ E-mail: zhao13@ualberta.ca

(BY Draconis) or evolved stars (RS CVn), make up the majority of faint X-ray sources below 10^{31} erg s^{-1}, and are mostly formed primordially (Grindlay et al. 2001a; Bassa et al. 2004).

1.1 Radio sources in globular clusters

Thanks to the increased sensitivity of new Karl G. Jansky Very Large Array (VLA) and Australia Telescope Compact Array (ATCA) receivers, faint radio sources have been detected in a number of GCs (e.g. Strader et al. 2012; Chomiuk et al. 2013; Miller-Jones et al. 2015). There are several possibilities for these sources.

NS LMXBs in the low/hard states produce flat ($-0.5 < \alpha < 0$; $S_\nu \propto \nu^\alpha$) to inverted ($\alpha \geq 0$) radio spectra, thought to be from jets, correlated with their X-ray luminosity (Migliari & Fender 2006; Tudor et al. 2017; Gusinskaia et al. 2020). Black hole (BH) LMXBs produce jets with similar radio spectra, but the radio luminosity is significantly higher for a given X-ray luminosity (Gallo et al. 2014; Gallo, Degenaar & van den Eijnden 2018; Plotkin et al. 2019a). Millisecond radio pulsars generally show steep spectral indices, with a mean of $\alpha = -1.4$ and unit standard deviation (Bates, Lorimer & Verbiest 2013).

Non-magnetic[1] CVs show flat-to-inverted radio spectra during accretion episodes, believed to be synchrotron emission from a jet (Benz, Fuerst & Kiplinger 1983; Körding et al. 2008; Miller-Jones et al. 2013; Coppejans et al. 2015, 2016; Russell et al. 2016). Numerous magnetic CVs have been detected in the radio, though a number of magnetic CVs show circular polarization indicative of electron–cyclotron maser emission (Chanmugam 1987; Abada-Simon et al. 1993; Barrett et al. 2017). This maser emission has been suggested to be produced near the companion star (Mason & Gray 2007), or to be produced near the WD (Kurbatov, Zhilkin & Bisikalo 2019). Radio luminosities for all CVs tend to be rather low (tens to hundreds of μJy at 300 pc; e.g. Coppejans et al. 2016), except during brief flares within dwarf nova outbursts (Mooley et al. 2017). The most radio-luminous WDs known are the extreme magnetic CV AE Aquarii, which is thought to eject much of the infalling matter through a propeller (Wynn, King & Horne 1997; Meintjes & Venter 2005), and the WD pulsar AR Sco, where the WD does not accrete, but produces non-thermal emission from the radio through X-ray (Marsh et al. 2016).

ABs are also radio sources, though generally they are not luminous enough for detection at kpc distances except during short (hours) flares (Drake, Simon & Linsky 1989; Osten et al. 2000). Tidal interaction in close orbits leads to synchronized rotation with short orbital period and thus strong coronal magnetic activity (Chugainov 1966; Bailyn et al. 1990; Dempsey et al. 1993). The emission mechanism is generally attributed to gyrosynchrotron radiation of mildly relativistic electrons interacting with photospheric magnetic fields (Hjellming & Gibson 1980; Feldman 1983; Kundu & Shevgaonkar 1985; Gudel 1992). They are generally observed to be non-thermal, highly variable, and circularly polarized with flat or negative spectral indices ($\alpha \lesssim 0$; García-Sánchez, Paredes & Ribó 2003). An unusual system, a sub-subgiant[2] in a binary with either a very low mass star or else a more massive compact object (possibly a BH) in an extremely face-on binary, is a radio and X-ray source in the GC M10 (Shishkovsky et al. 2018).

1.2 Eclipsing millisecond pulsars

MSPs are often in close orbits with very low mass (as low as $\sim$0.02 M$_\odot$) stars. If the companion is not fully degenerate, it may produce an outflowing wind, which interacts with the pulsar wind to create an intrabinary shock. The pulsar's radiation and/or accelerated particles may heat the companion's surface, enhancing the companion's wind. This enhanced companion wind, and/or the intrabinary shock, may eclipse the radio pulsations. These systems fall into two major categories, 'black widow' systems with brown dwarf companions of $\lesssim$0.02 M$_\odot$ (Fruchter, Stinebring & Taylor 1988; Stovall et al. 2014) and 'redback' systems with main-sequence (MS) companions of typically $\sim$0.1–0.4 M$_\odot$ (Lyne et al. 1990; Ferraro et al. 2001; Roberts 2013), but possibly higher companion masses up to 0.7–0.9 M$_\odot$ (Strader et al. 2019). The radio eclipses are often seen to encompass 10–25 per cent of the full orbit, but the eclipse lengths can vary between orbits, and at low frequencies some systems appear to be permanently eclipsed (e.g. Camilo et al. 2000; Freire 2005; Polzin 2020). There are also MSPs such as 47 Tuc V that show irregular eclipses at all orbital phases and are sometimes not detected for many orbits, suggesting they are continuously eclipsed (Camilo et al. 2000; Ridolfi et al. 2016). It is speculated that many MSPs may be continuously hidden behind even stronger winds (Tavani 1991).

The mechanism by which the wind from the companion star causes eclipses in the radio pulsations is not clear. The radio pulses typically show increased dispersion near the eclipse, and/or become substantially fainter (Stappers et al. 2001; Archibald et al. 2009). Thompson et al. (1994) discuss a range of possible mechanisms, including free–free absorption, pulse smearing, scattering due to Langmuir turbulence, stimulated Raman scattering, and cyclotron absorption. Thompson et al. (1994) and later works (Stappers et al. 2001; Polzin et al. 2019) typically favour cyclotron absorption and/or scattering mechanisms, while some works (Broderick et al. 2016; Polzin et al. 2018) strongly favour cyclotron absorption to explain eclipses, especially at low (e.g. 300 MHz) frequencies. Fruchter & Goss (1992) imaged PSR 1957+20 through eclipses at both 20 and 90 cm with the VLA, discovering that the unpulsed flux disappeared during eclipse at 90 cm but was still present at 20 cm, suggesting cyclotron absorption at low frequencies and scattering at higher frequencies (Thompson et al. 1994). The LOFAR array has been used to image pulsars during eclipses, where the disappearance of the flux at e.g. 149 MHz was seen, in agreement with cyclotron absorption scenarios (Roy et al. 2015; Broderick et al. 2016; Polzin et al. 2018).

Observations of lengthy X-ray eclipses in redbacks were initially understood as a direct eclipse by the secondary star of X-ray emission from an intrabinary shock, located close to the secondary (Bogdanov, Grindlay & van den Berg 2005). However, higher signal-to-noise ratio (S/N) orbital X-ray light curves of eclipsing pulsars have revealed modulation of the X-rays throughout the orbit, and sharp peaks, often on either side of the inferior conjunction of the NS (e.g. Bogdanov et al. 2011, 2014; Romani & Shaw 2011; Huang et al. 2012; Hui et al. 2014, 2015; de Martino et al. 2015). This has inspired interpretation of the X-rays as due to particle acceleration at the interface between the companion and pulsar winds, beamed in the direction of the particle flow (e.g. Harding & Gaisser 1990; Arons & Tavani 1993; Romani & Sanchez 2016; Wadiasingh et al. 2017). The very hard X-ray photon index rules out

[1]CVs are divided into magnetic systems, where the WD magnetic field is strong enough ($B \sim 10^6$–10^8 G) to channel the accretion on to magnetic poles, and non-magnetic systems where an accretion disc reaches the surface.
[2]A star fainter than subgiants but redder than the MS; see Leiner, Mathieu & Geller (2017).

shock acceleration, suggesting magnetic reconnection in a striped pulsar wind (e.g. Al Noori et al. 2018). It is unclear how the intrabinary shock manages to wrap around the pulsar; suggested scenarios are that the companion wind is highly magnetized (as the companion is likely magnetically active; van Staden & Antoniadis 2016) and thus that the companion wind balances the pulsars via magnetic pressure, or that the companion wind is dense enough for its gas pressure to balance the pulsar wind's magnetic pressure (Wadiasingh et al. 2018). The latter case is inherently unstable to gravity if the intrabinary shock bends around the pulsar, which may explain rapid transitions between accretion and pulsar states (Papitto et al. 2013). We note that Li et al. (2019) place very constraining upper limits on the B field at the interface between the pulsar and companion winds in PSR B1957+20, casting doubt on the cyclotron absorption eclipse scenario and the magnetospheric pressure balance scenario.

1.3 NGC 6397

NGC 6397 has been intensively observed by optical, X-ray, and radio instruments as a nearby GC with relatively low extinction ($D \approx 2.3$ kpc; $E(B-V) = 0.18$; Harris 1996, 2010 edition). Ferraro et al. (2001) identified an eclipsing MSP, PSR J1740−5340 (aka NGC 6397-A), the second discovered 'redback' MSP, in NGC 6397. Grindlay et al. (2001b) used 49 ks of *Chandra*/ACIS-I observation to reveal 25 X-ray sources within 2 arcmin of the cluster, and used *Hubble Space Telescope* (*HST*) imaging to identify eight CVs and four ABs. Grindlay et al. (2001b) identified PSR J1740−5340 as an X-ray source (U12), and suggested that the similar (in X-ray and optical properties) source U18 might be a hidden MSP. Bogdanov et al. (2010) performed a much deeper search for X-ray sources in 350 ks of *Chandra* observations, finding 79 sources. Cohn et al. (2010) used new *Hubble* imaging to increase the totals for NGC 6397 to 15 CVs and 42 ABs.

In this work, we present our detections of radio counterparts to U12, U18, two previously known faint X-ray sources (U97 and U108), and three newly detected X-ray sources (W127, W129, and W135). In Section 2, we describe the observational data and relevant methodologies of data reduction; in Section 3, we present results from cross-matching X-ray with radio catalogues and discuss individual matches; in Section 5, we summarize results and draw conclusions, and in Appendix A, we present an updated X-ray catalogue and tentative identifications of the new sources.

2 OBSERVATIONS AND ANALYSES

2.1 Radio observations

NGC 6397 was observed by the Australia Telescope Compact Array (PI: Strader) as part of the MAVERIC (Milky Way ATCA and VLA Exploration of Radio sources In Clusters) survey (project code: C2877; Shishkovsky et al. 2018; Tremou et al. 2018). The observation started on 2013 November 9 (exact times MJD 56605.94–56606.39 and 56606.96–56607.38) with two radio bands centred at 5.5 and 9 GHz (both with 2 GHz of bandwidth) in the extended 6A configuration, for a total observational time of 20 h and a total on-source integration time of 16.2 h. Calibration and image analysis were done with MIRIAD (Sault, Teuben & Wright 1995) and CASA (version 4.2.0; McMullin et al. 2007), rendering radio images at noise levels of 4.22 and 4.81 μJy per beam. We used the standard source PKS 1934−638 as both bandpass and flux calibrator, and the nearby source 1740−517 as our secondary calibrator, to determine the time-varying amplitude and phase gains that were then linearly interpolated to the target field. To achieve a high sensitivity, we applied the Briggs weighting scheme, with a robust parameter of 1, resulting in synthesized beam sizes of 1.54 arcsec × 2.80 arcsec and 1.03 arcsec × 1.87 arcsec at 5.5 and 9 GHz, respectively. Since there was not sufficient flux density in the field, no self-calibration was done. The radio positional accuracy directly obtained from this procedure is overestimated, so we inflate the source position uncertainties to at least 1/10 the 5.5/9 GHz beam sizes.

We derive spectral indices (α), defined by $S_\nu \propto \nu^\alpha$, using a Bayesian approach. We assume a flat prior of α between −3.5 and 1.5 and calculate the posterior distribution for each radio source, from which we derive a median and an associated uncertainty range that covers 68 per cent of the total area. For sources that were not detected at 9 GHz (so only upper limits to the fluxes are available), we report 3 σ upper limits on α derived from the posterior distribution; medians are also calculated for these sources but are very sensitive to the prior, especially to the assumed lower bound (−3.5), so should be interpreted with caution.

More details on the procedure of generating 5 σ radio source catalogues will be presented in a separate work (Tudor et al., in preparation).

2.2 X-ray observations

We used the same *Chandra* data set as in Bogdanov et al. (2010), including an ACIS-I observation from Cycle 1 (Obs. ID: 79; PI: Murray) and ACIS-S observations from Cycle 3 (Obs. IDs: 2668, 2669; PI: Grindlay) and Cycle 8 (Obs. IDs: 7460, 7461; PI: Grindlay). All level-1 files are first reprocessed to align to the most up-to-date calibrations using the `chandra_repro` script in the Chandra Interactive Analysis of Observations (CIAO; Fruscione et al. 2006)[3] software (version 4.11; CALDB 4.8.2). The resulting level-2 event files were used for further analyses. We then chose the longest observation (Obs. ID 7460) as the reference frame, to which we calculated relative offsets for all other observations based on the centroid positions of U17, the brightest source in the catalogue. These offsets were then used as input to the `wcs_update` tool to update aspect solutions for each observation. Finally, all offsetted event files were combined using the `merge_obs` tool, rendering a combined event file. We then rebinned the combined event file to a quarter of an ACIS pixel (0.25 arcsec) and applied an energy filter of 0.5–7 keV to generate an X-ray image.

To get source positions, we run `wavdetect` on a 400 arcsec × 400 arcsec image centred on the cluster. We used size scale parameters of 1, 1.4, 2.0, and 2.8, while setting the threshold significance parameter to 3.9×10^{-7}. This value is the reciprocal of the number of pixels in the image, to minimize misidentifications of background fluctuations as sources.[4] The `wavdetect` positions are then corrected for boresight offsets (Section 2.3) before being cross-matched with our radio catalogues.

We searched for point sources within the half-light radius (=2.9 arcmin) derived by Harris (1996, 2010 edition), which is somewhat greater than that (=2.33 arcmin) used by Bogdanov et al. (2010). As a result, our `wavdetect` run revealed a total of 23 point sources that are not previously catalogued, of which 18 are outside the 2.33 arcmin radius and 5 are inside (Fig. 1). Some of these new sources are found to be positionally consistent with

[3] https://cxc.harvard.edu/ciao/
[4] http://cxc.harvard.edu/ciao/threads/wavdetect/

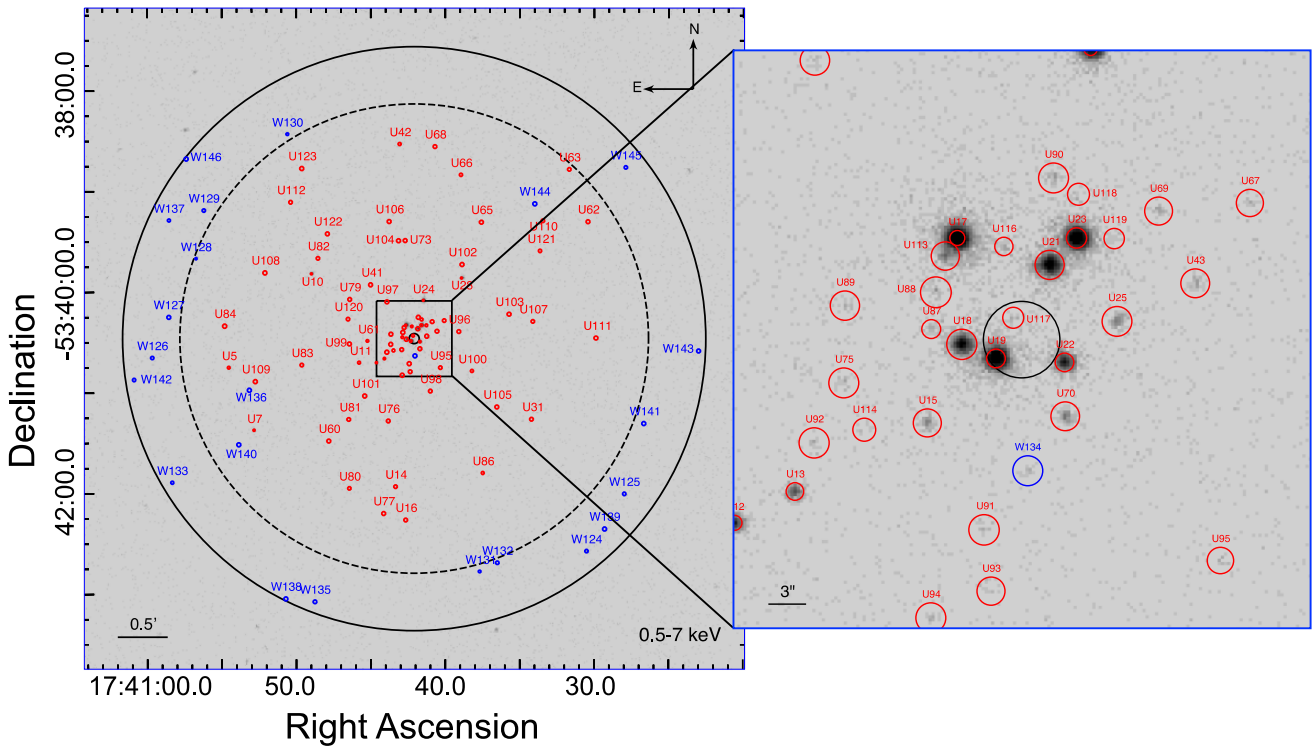

Figure 1. *Left:* 0.5–7 keV X-ray image of a 6.6 arcmin × 6.6 arcmin square region centred on the cluster. North is up and east is to the left. New sources detected by `wavdetect` (blue) and sources from Bogdanov et al. (2010) (red) are marked by circles that enclose 90 per cent of their point spread functions. The solid black circle shows the 2.9 arcmin half-light radius (r_h), while the dashed black circle depicts the 2.33 arcmin searching radius used in Bogdanov et al. (2010). *Right:* A zoomed-in 45 arcsec × 45 arcsec square region centred on the cluster. The solid black circle shows the 0.05 arcmin core radius (r_c).

our radio sources (Section 3); moreover, X-ray positions derived from better astrometry with the *Gaia* Catalogue of Data Release 2 (DR2) result in sub-arcsecond scale offsets (Section 2.3). We thus report an extended X-ray catalogue with updated source coordinates including both old and new sources (Appendix A). To distinguish from the old sources, the new sources are named with 'W' + sequential ID starting from 124, which are all summarized in Table A1. For each new X-ray source, we run the CIAO `srcflux` script to calculate the X-ray counts in soft (0.5–1.5 keV) and hard (1.5–6 keV) bands, and based on the total counts, we calculated 95 per cent error radii ($P_{\rm err}$) using an empirical formula from Hong et al. (2005).

For sources with radio counterparts, we also extracted X-ray spectra using the CIAO `specextract` script and performed analyses using the HEASOFT/XSPEC software (version 12.10.1; Arnaud 1996).[5] We combined the ACIS-S spectra for each source using the HEASOFT/FTOOLS `addspec` task to maximize spectral counts, and then rebinned the bright ($\gtrsim$700 counts between 0.5 and 6 keV) source spectra (U12 and U18) to at least 20 counts per energy bin, and faint spectra (U97, U108, W25, W129, and W135) to at least 1 count per bin. The former are then modelled using the χ^2 statistic, and the latter with the *C*-statistic (Cash 1979). Since ACIS's sensitivity falls off at low energies, we only use energy channels between 0.5 and 10 keV in all of our fits. We note that the spectra of U12 and U18 have been well analysed by Bogdanov et al. (2010). We thus adopt the corresponding best-fitting models (power laws for U12 and U18) and calculate X-ray fluxes between 1 and 10 keV, which will be further used in Section 3. We fit the faint source spectra to absorbed power-law models using `wilms` abundances (Wilms, Allen & McCray 2000), keeping the absorption column density ($N_{\rm H}$) fixed at the cluster value ($\approx$1.57 × 10^{21} cm^{-2}, derived using $E(B-V) = 0.18$ from Harris 1996 and a conversion factor from Bahramian et al. 2015). For W129, we obtained relatively more counts (111 counts between 0.5 and 10 keV), so we fit its spectrum allowing $N_{\rm H}$ to be free.

[5] https://heasarc.gsfc.nasa.gov/xanadu/xspec/

2.3 *HST* observations and astrometry

For absolute astrometry, we used data from observations by the *HST*/Advanced Camera for Surveys (ACS) in the F625W band (R_{625}). The separate exposures are in the form of 'FLC' images that are pipelined, flat-fielded, and cleaned for charge transfer efficiency trails. We used the `Tweakreg` and `Astrodrizzle` tasks in the DRIZZLEPAC software package to align and combine the individual FLC frames. We set the `pixfrac` to 1.0 and the final pixel size to 0.025 arcsec, oversampling the resulting image by a factor of 2.

We then aligned the resulting 'drizzle'-combined image to a catalogue with superior astrometry and used it as the reference frame. For this purpose, we chose stars that have relatively low astrometric uncertainties [with error in right ascension (RA) and declination (Dec.) $\leq$0.05 mas] from the *Gaia* DR2 (Gaia Collaboration 2016, 2018a). These stars are matched with stars in the F625W frame, so we can calculate averaged relative offsets. We found 50 such stars within a searching radius of 1.2 arcmin centred on the cluster, resulting in average offsets (*Gaia* − ACS) of 1.53 ± 0.03 and 1.28 ± 0.01 arcsec in RA and Dec. (1 σ errors), respectively. We consider boresight correction for the catalogue by calculating relative offsets (ACS − *Chandra*) between the X-ray centroids and

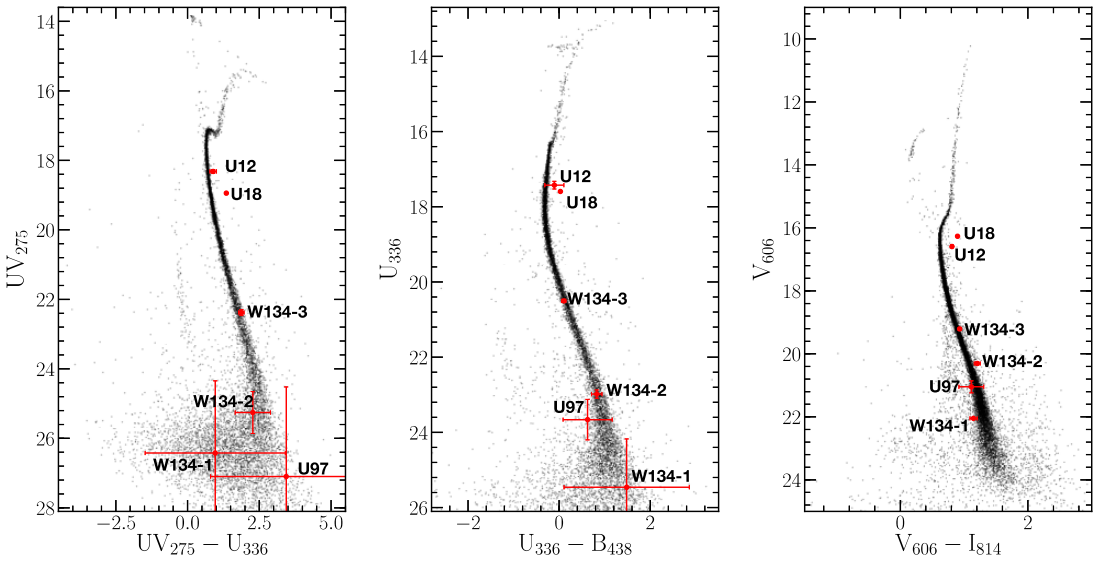

Figure 2. CMDs of stars from the HUGS catalogue. Locations and errors of optical/UV counterparts to X-ray sources with radio counterparts are indicated with red points and bars. We also present the photometry of three objects that lie within the 95 per cent error circle of W134, a new X-ray source with HUGS data available (see also Appendix A).

Table 1. Positional information of radio–X-ray cross-matched sources.

Source ID	X-ray position		$P^a_{\rm err}$	Radio position[b]		Optical position[c]		P^d_μ
	$\alpha_{\rm X}$	$\delta_{\rm X}$	(arcsec)	$\alpha_{\rm R}$	$\delta_{\rm R}$	$\alpha_{\rm O}$	$\delta_{\rm O}$	(per cent)
U12	17:40:44.63	−53:40:42.0	0.30	17:40:44.64(1)	−53:40:41.9(3)	17:40:44.629	−53:40:41.94	97.9
U18	17:40:42.62	−53:40:28.0	0.29	17:40:42.63(1)	−53:40:28.1(3)	17:40:42.626	−53:40:27.91	98.3
U97	17:40:43.92	−53:40:05.7	0.44	17:40:43.94(1)	−53:40:05.7(3)	17:40:43.927	−53:40:05.89	97.5
U108	17:40:52.11	−53:39:48.4	0.46	17:40:52.16(1)	−53:39:48.7(3)	17:40:52.168	−53:39:48.79	–
W127	17:40:58.56	−53:40:14.9	0.52	17:40:58.51(2)	−53:40:15.5(3)	–	–	–
W129	17:40:56.20	−53:39:11.2	0.35	17:40:56.21(1)	−53:39:11.1(3)	17:40:56.192	−53:39:10.882	–
W135	17:40:48.75	−53:43:04.4	0.64	17:40:48.74(1)	−53:43:05.4(3)	–	–	–

[a]95 per cent error radii of X-ray positions; see Hong et al. (2005).
[b]The uncertainties in the $\alpha_{\rm R}$ and $\delta_{\rm R}$ are derived from projections of the radio error ellipses (Section 2) to the RA and Dec. axes.
[c]Uncertainties in optical positions are mostly from astrometry (Section 2.3).
[d]Membership probabilities from the HUGS catalogue; see Nardiello et al. (2018).

positions of the identified counterparts for the three brightest CVs (U17, U19, and U23), from which we obtained average offsets in RA and Dec. of −0.09 and −0.13 arcsec, respectively. These offsets are applied to the combined *Chandra* image used for making finding charts.

We also incorporate results from the *HST* UV Globular Cluster Survey (HUGS; Piotto et al. 2015; Nardiello et al. 2018) into our analyses, which provides photometry in three *HST*/WFC3 bands: F275W (UV_{275}), F336W (U_{336}), and F438W (B_{438}); and two *HST*/ACS bands: F606W (V_{606}) and F814W (I_{814}). The latter are adapted from the ACS Survey of Galactic Globular Clusters (GO-10775, PI: Sarajedini; Sarajedini et al. 2007; Anderson et al. 2008). We plotted three colour–magnitude diagrams (CMDs) using stars that have good photometric measurements in multiple filters (Fig. 2). Locations of interesting sources on the CMDs provide useful information in our further discussions (Section 3).

3 RESULTS

By cross-matching the 5 σ radio catalogue with our updated X-ray catalogue, we sought radio sources that lie within $P_{\rm err}$, and found seven radio sources positionally coincident with *Chandra* sources, including U12 (PSR 1740−5340), U18, U97, U108, and three new sources (W127, W129, and W135) that are likely active galactic nuclei (AGNs). We found U24, the quiescent LMXB, may be associated with a faint extension to a bright source in the 5.5-GHz image, so we also include it in our discussions. In Table 1, we summarize the positional information of these sources, and in Fig. 3, we show the corresponding X-ray, radio, and optical finding charts. In Table 2, we present 1–10 keV X-ray fluxes (from spectral fits described in Section 2.2), and in Fig. 4, we plot the 5-GHz radio versus 1–10 keV X-ray luminosities for cluster sources assuming flat ($\alpha = 0$) radio spectra, together with other classes of accreting compact objects.

3.1 U12, PSR J1740−5340

PSR J1740−5340 was discovered by the Parkes telescope as part of a 1.4-GHz radio timing survey for GC MSPs (D'Amico et al. 2001a, b). Irregular radio eclipses were found for more than 40 per cent of its ∼33-h orbit. The X-rays also show a decrease during the radio eclipse, which was interpreted as occultations by the companion star of the shock front produced by interaction between pulsar winds and outflowing mass from the companion (Bogdanov et al. 2010).

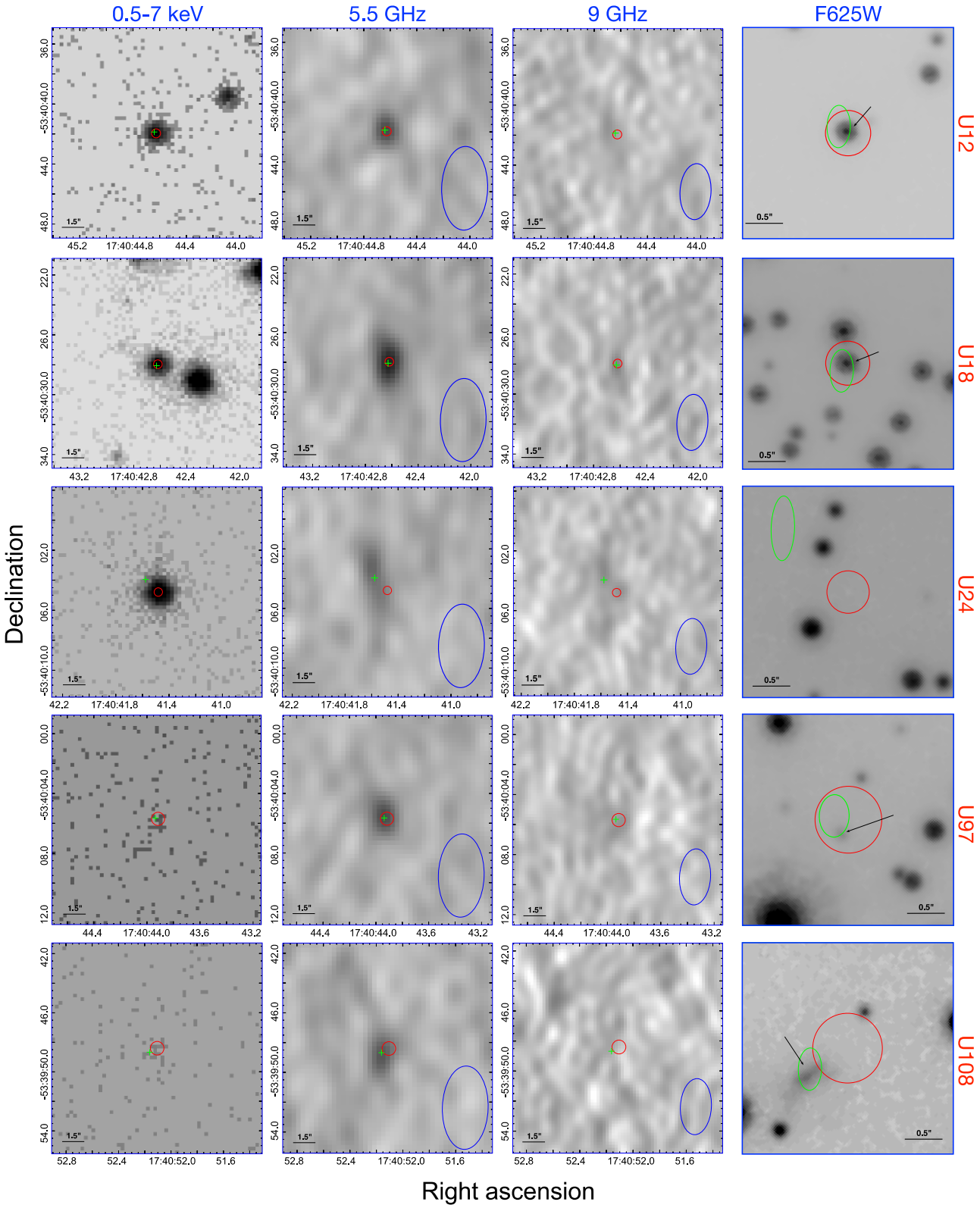

Figure 3. X-ray (0.5–7 keV), radio (5.5 and 9 GHz), and optical (F625W) finding charts for U12, U18, U24, U97, and U108. North is up and east is to the left. The X-ray and radio charts are all 14 arcsec × 14 arcsec in size, while the F625W finding charts are 2.8 arcsec × 2.8 arcsec. We show the 95 per cent *Chandra* error region with red circles. Since the radio sources have relatively small positional uncertainties, we only show their nominal positions with green crosses in the X-ray and radio images, while in the somewhat zoomed-in F625W charts, we show radio error regions with green ellipses (the sizes of which are described in Section 2) and indicate the optical counterparts with black arrows. The radio beams in the radio charts are shown with blue ellipses on the bottom right of the 5.5- and 9-GHz images. The top two rows show X-ray (0.5–7 keV) and radio (5.5 and 9 GHz) finding charts for W127 and W135. The last row shows X-ray, radio, and infrared (F160W) finding charts for W129. The 5.5/9-GHz and the F160W charts are 12 arcsec × 12 arcsec and 5.5 arcsec × 5.5 arcsec in size, respectively. Radio error regions are shown with green ellipses..

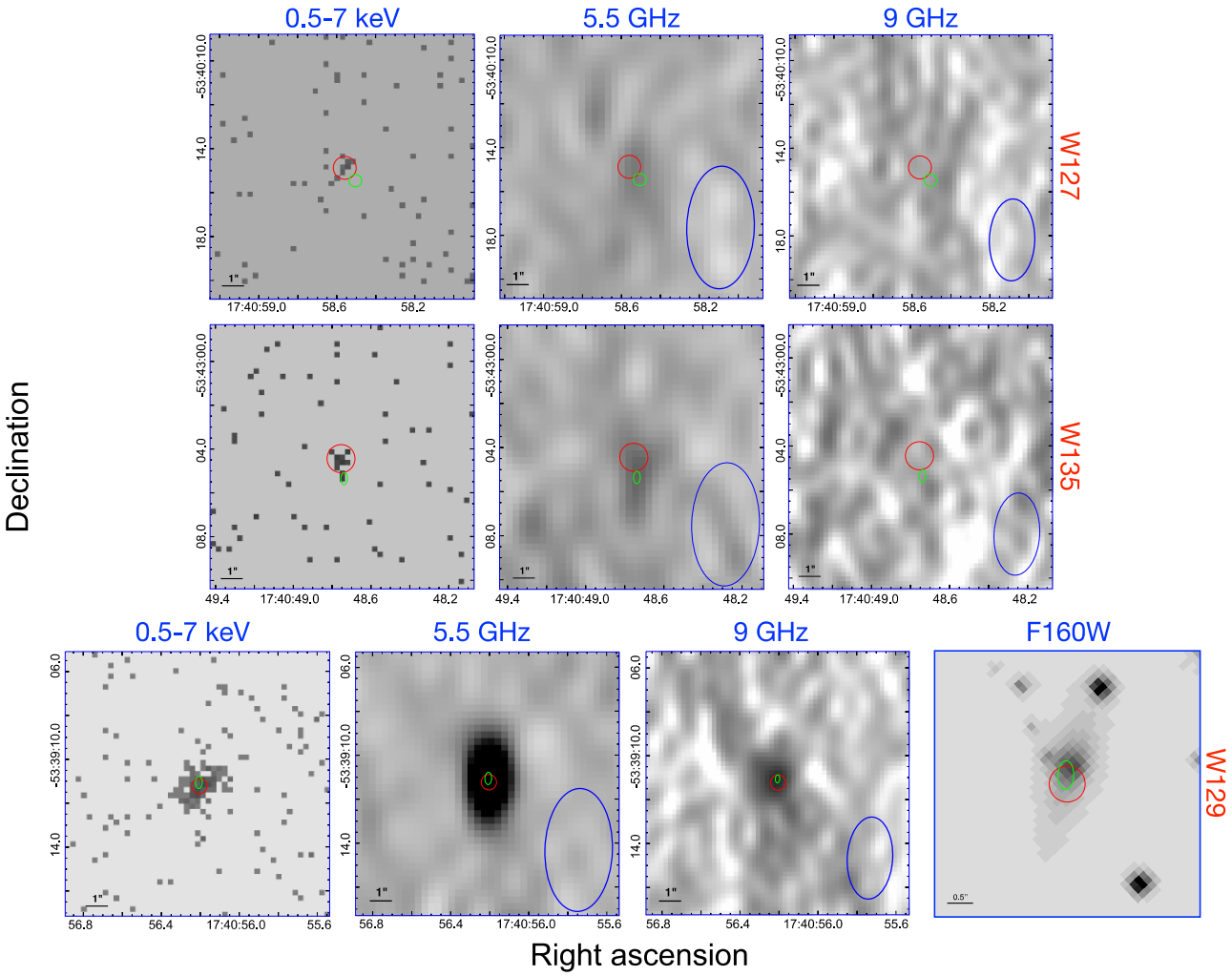

Figure 3 – *continued*

Table 2. Radio and X-ray properties of sources in Table 1.

ID	F_X ($\times 10^{-16}$ erg s^{-1} cm^{-2}) (1–10 keV)	Photon index (Γ)[a] ($F_X \propto E^{-\Gamma}$)	S_ν (μJy) 5.5 GHz	9 GHz	Spectral index (α)[b] Median	3 σ upper limit	Comment
U12	$250.4^{+14.8}_{-14.8}$	$1.7^{+0.2}_{-0.2}$	36.7 ± 4.4	<25.0	$-2.1^{+1.1}_{-1.0}$	<0.5	MSP
U18	$990.6^{+32.9}_{-33.0}$	$1.3^{+0.1}_{-0.2}$	54.7 ± 4.3	21.6 ± 4.4	$-2.0^{+0.4}_{-0.5}$	–	MSP?
U97	$11.8^{+7.3}_{-5.6}$	$0.5^{+1.0}_{-1.0}$	34.1 ± 4.7	18.6 ± 4.5	$-1.3^{+0.6}_{-0.7}$	–	AB or BH?
U108	$5.3^{+2.4}_{-1.9}$	$1.9^{+0.8}_{-0.7}$	34.9 ± 4.5	<26.8	$-2.0^{+1.2}_{-1.0}$	<0.7	Galaxy
W127	$7.2^{+4.6}_{-3.3}$	$1.1^{+1.0}_{-1.0}$	26.9 ± 5.0	<35.8	$-1.5^{+1.5}_{-1.3}$	<1.0	AGN?
W129	$416.8^{+72.3}_{-64.9}$	$2.7^{+1.4}_{-1.2}$	163.0 ± 5.0	65.0 ± 8.9	$-1.9^{+0.3}_{-0.3}$	–	Galaxy
W135	$19.8^{+11.8}_{-8.7}$	$-0.2^{+1.0}_{-1.2}$	31.5 ± 5.8	<39.4	$-1.6^{+1.4}_{-1.3}$	<1.0	AGN?

[a]X-ray photon indices derived from spectral fits to a power-law model (Section 2.2).
[b]Radio spectral indices derived using a Bayesian approach; see Section 2.1.

In the optical, a sub-subgiant with $M \sim 0.3$ M$_\odot$ was identified as the counterpart to this MSP (Ferraro et al. 2001; Kaluzny, Rucinski & Thompson 2003; Orosz & van Kerkwijk 2003). Further optical spectroscopic studies of this sub-subgiant revealed asymmetric line features and ellipsoidal photometric variations, indicating that the companion fills its Roche lobe (Orosz & van Kerkwijk 2003), and that it is heated by a beam of radiation from the pulsar (Ferraro et al. 2003; Sabbi et al. 2003).

Consistently, we found the optical counterpart to U12 appears to be in the sub-subgiant region on all three HUGS CMDs (Fig. 2). There is no sign of strong UV emission, indicating the absence of a hot disc. This is consistent with the picture suggested by Bogdanov et al. (2010) where matter flows from the companion towards the NS, never reaches the NS, but rather is halted and swept back by the strong pulsar wind, forming an intrabinary shock.

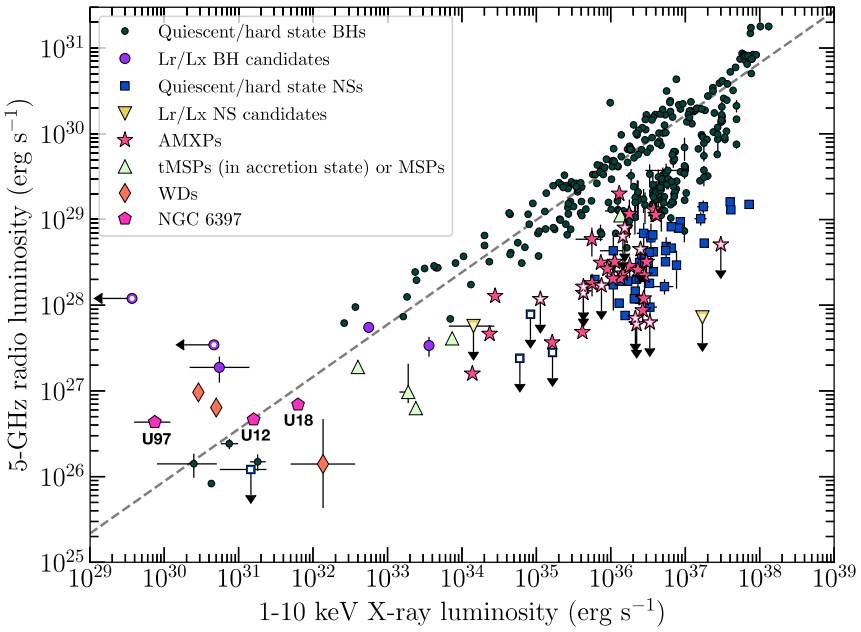

Figure 4. 5-GHz radio luminosities plotted versus 1–10 keV X-ray luminosities for different classes of accreting compact objects. X-ray sources in NGC 6397 associated with radio counterparts are shown with filled pentagons. The radio luminosities are calculated assuming flat ($\alpha = 0$) spectra. The deep green circles represent known quiescent BHs (Soleri et al. 2010; Miller-Jones et al. 2011; Gallo, Miller & Fender 2012; Ratti et al. 2012; Corbel et al. 2013; Rushton et al. 2016; Plotkin et al. 2017). The dashed grey line shows the L_R–L_X correlation for BHs from Gallo et al. (2014). The larger purple circles are radio-selected BH candidates (Strader et al. 2012; Chomiuk et al. 2013; Miller-Jones et al. 2015; Tetarenko et al. 2016; Bahramian et al. 2017; Shishkovsky et al. 2018). The light green triangles mark known transitional MSPs (Hill et al. 2011; Papitto et al. 2013; Deller et al. 2015; Bogdanov et al. 2018). The deep blue squares and pink stars show quiescent/hard-state NSs and accreting millisecond X-ray pulsars (AMXPs), respectively (Migliari & Fender 2006; Tudor et al. 2017). The yellow triangles show upper limits of L_R of two X-ray transients (Tetarenko et al. 2016; Ludlam et al. 2017). The orange diamonds mark radio detected bright WDs, including AE Aqr (Eracleous, Halpern & Patterson 1991; Abada-Simon et al. 1993), SS Cyg (at flare peak; Russell et al. 2016), and AR Sco (a radio-pulsating WD; Marsh et al. 2016). The hollow markers indicate upper limits. For script and data used to generate the plot, see Bahramian et al. (2018).

We found an 8 σ ATCA source 0.15 arcsec ($\approx$0.5 $P_{\rm err}$) from the nominal X-ray position of U12 (Fig. 3), with a 5.5-GHz flux density of 36.7 $\pm$ 4.4 μJy. The 9-GHz observation reveals an upper limit of 25 μJy, so we obtain a rough 3 σ constraint on the spectral index of $<$0.5 (see Section 2.1).

We then imaged the ATCA 5.5-GHz data in two (similar-length) parts, inside and outside the eclipse phases. To calculate the eclipse phases, we used the eclipse phases of 0.05–0.45 quoted in D'Amico et al. (2001a), the orbital period of 1.35405939(5) d from D'Amico et al. (2001b), and a T0 from Mucciarelli et al. (2013) of MJD 52413.22761, to give relevant eclipse times of MJD 56605.44−56605.98 and 56606.79−56607.33. The out-of-eclipse image detects U12 at 58.3 $\pm$ 5.1 μJy, while the in-eclipse image does not detect U12, with a 3 σ upper limit of 19 μJy.

Comparing the out-of-eclipse flux density to the 1.4-GHz flux density of $S_\nu \sim$ 0.5–1.5 mJy measured by the Parkes radio telescope (D'Amico et al. 2001a; we assume this value is outside the eclipse only) constrains the spectral index $-2.4 \lesssim \alpha \lesssim -1.6$, within the range of steep spectral indices observed in radio pulsars (Bates et al. 2013). We also created images in Q, U, and V Stokes parameters, but did not see evidence of polarized emission. The 3 σ upper limit of 16.5 μJy per beam indicates a polarization upper limit of 28 per cent.

3.2 U18: a hidden MSP?

Grindlay et al. (2001b) discovered the X-ray source U18, associated it with a sub-subgiant counterpart (see also Cohn et al. 2010), and suggested, given the similarities in X-ray and optical properties to PSR J1740−5340 (U12), that U18 is also a redback MSP, where, in this case, the eclipsing wind completely (or near-completely) blocks the observability of radio pulsations. Bogdanov et al. (2010) confirmed U18's hard non-thermal spectrum ($\Gamma \approx 1.3$) and variability on time-scales from hours to years, which are consistent with a shocked-wind MSP origin for the X-ray emission. Cohn et al. (2010) confirmed that U18's proper motion (PM) marked it as a cluster member, and identified strong optical variability from U18 ($\sigma \sim 0.03$ mag).

U18 has a definite match with an 11.7 σ radio source 0.13 arcsec ($\approx$0.4$P_{\rm err}$) from the nominal X-ray position in our 5.5-GHz radio image (Fig. 3). The source was also detected in 9 GHz, allowing us to measure its spectral index, $\alpha = -2.0^{+0.4}_{-0.5}$. The steep radio spectrum is consistent with observations of many MSPs (Sieber 1973; Lorimer et al. 1995; Bates et al. 2013). Breaking the 5.5-GHz data into 2 d of similar exposures gives flux densities of 67 $\pm$ 5 and 40 $\pm$ 6 μJy, confirming variability (at 3.5 σ significance), but not indicating extreme flaring. Searching for polarization gave a 3 σ upper limit of 25 per cent polarized emission (similar to U12 above). We also confirm the sub-subgiant position of U18 in all three CMDs, including the UV HUGS data (Fig. 2).

Could U18 be something other than an MSP? The radio and X-ray luminosities of U18 are compatible with quiescent BHs (e.g. Gallo et al. 2014). However, the steep radio spectral index of U18 strongly disfavours this scenario, in that quiescent BHs generally have flat-to-inverted radio spectra.

U18's steep radio spectral index and high radio luminosity ($L_R \approx 6.9 \times 10^{26}$ erg s^{-1} at 5.5 GHz, if one incorrectly assumes a flat radio spectrum) without short, bright flares set its radio emission

apart from the CV behaviour discussed in Section 1.1. Nor do the unusual systems AE Aqr (a propeller system) or AR Sco (a WD pulsar) match U18's spectral index, or AE Aqr's flaring behaviour. The optical counterpart to U18 exhibits a moderate H α excess and a relatively low X-ray/optical ratio, which are both consistent with typical GC CVs (e.g. Cohn et al. 2010). However, U18 completely lacks (Fig. 2) the UV or blue excesses that originate from the hot accretion disc and/or WD surface in typical CVs. Marked optical/UV variabilities are common in some CVs, which might alter UV flux by up to 1 mag on time-scales of hours (see e.g. Rivera Sandoval et al. 2018), but cannot be responsible for the strong red excesses of U18 observed in all three CMDs. Considering the radio and UV/optical data, we rule out a CV interpretation for U18.

Finally, an AB interpretation cannot be completely ruled out (as the radio spectral index is reasonable; García-Sánchez et al. 2003). The radio luminosity ($L_{\rm R} = 6.9 \times 10^{26}$ erg s^{-1}) can be reached by strong flares in some RS CVn systems (see e.g. García-Sánchez et al. 2003), but is far above the steady radio luminosities seen for known low-mass ABs (see e.g. Guedel & Benz 1993).

Thus, the evidence points to a hidden MSP in U18. Non-detection of pulsations in 1.4- and 3-GHz searches,[6] if confirmed, generally could imply an unfavourable beaming geometry, but the detection of a bright, steep-spectrum 5.5-GHz source is strong evidence that we are seeing radio pulsar emission from U18. It is possible that U18 shows pulsations at 5.5 GHz while being completely eclipsed at 3 GHz, so we do encourage higher frequency pulsar searches of NGC 6397. However, this seems unlikely; we conclude that U18 is an MSP whose pulsations may have been completely eclipsed in all observations and frequencies used so far. We discuss the eclipse mechanism further in Section 4.

3.3 U24–radio related to a quiescent LMXB?

U24 is a quiescent LMXB containing an NS (Grindlay et al. 2001a; Guillot, Rutledge & Brown 2011; Heinke et al. 2014). Detection of radio emission from such an object would be unprecedented. A 6 σ flat-to-steep spectrum ($\alpha = -0.7^{+0.6}_{-0.6}$) ATCA source was found 1.2 arcsec ($\approx 4.3 P_{\rm err}$) north-east of the X-ray position. The relative astrometry indicates that this radio source is not associated with U24, nor with any other detectable X-ray or optical source. However, the radio source appears extended, and may have a faint ($\lesssim 3\sigma$) feature $\sim$1.5 arcsec south of the radio centroid that may overlap with the position of U24 (displaced by $\approx$0.2 arcsec, Fig. 3). This faint extension could be a separate source, though the data have too low significance to be sure. Deeper radio imaging of NGC 6397 would be needed to verify whether we indeed see radio emission from this quiescent NS.

3.4 U97

We found a 7.3 σ ATCA source 0.13 arcsec ($0.27 P_{\rm err}$) from the nominal X-ray position of U97, which shows a spectral index of intermediate steepness ($\alpha = -1.3^{+0.6}_{-0.7}$). Assuming the cluster distance and a flat spectrum, we estimate a 5.5-GHz radio luminosity of 4.3×10^{26} erg s^{-1}.

Cohn et al. (2010) found a faint ($V \approx (B + R)/2 \approx 21.9$) and moderately blue counterpart to U97, exhibiting prominent H α variability. Such variation is rare, so the suggested counterpart is highly likely to be the true counterpart. U97 is located fairly close ($\approx$0.5 arcsec or $\approx 0.2 r_{\rm h}$) to the cluster centre, and the suggested counterpart's PM matches the cluster, indicating a high membership probability (Nardiello et al. 2018; Table 1), so U97 is very likely a cluster member.

3.4.1 *A chromospherically active binary?*

The X-ray/optical ratio of this source overlaps with those of cluster ABs. The HUGS photometry yields a somewhat brighter V_{606} magnitude of 21.0 $\pm$ 0.2, suggesting significant variability. The observed V-band magnitude converts to an absolute magnitude (M_V) of 9.2, corresponding to a lower MS star of roughly 0.05 $L_\odot$ and $M \approx 0.54\,M_\odot$, according to the stellar models of Pecaut & Mamajek (2013). This suggests that U97 may be a BY Draconis variable, that is, an AB composed of two MS stars.

Guedel & Benz (1993) found that $\log(L_{\rm X}/L_{\rm R}) \lesssim 15.5$ for multiple types of ABs ($\approx$ applies for less luminous objects like BY Dra, while $<$ applies for more luminous classes such as RS CVn), suggesting that the heating of hot coronae (which emit X-rays) and the acceleration of particles (which emit in the radio) are closely related. Given the observed $L_{\rm X}$ ($\approx 7 \times 10^{29}$ erg s^{-1}, see Table 2), this correlation would predict $L_{\rm R}(8.5\ {\rm GHz}) \approx 2.4 \times 10^{14}$ erg s^{-1} Hz^{-1}, which is $\sim$3 orders of magnitude fainter than our observed 9-GHz luminosity. The X-ray and radio observations were not simultaneous, so conceivably the high radio luminosity could have been caused by flares at the time of the ATCA observations, while *Chandra* may have observed the source in a quiescent state. However, we found no clear sign of variability from comparing the two separate ATCA images. Furthermore, the radio luminosity ($L_{\rm R}(5.5\ {\rm GHz}) \approx 4.3 \times 10^{26}$ erg s^{-1}) we observe would be unparalleled for BY Dra systems. This scenario must be judged extremely unlikely.

3.4.2 *A quiescent BH X-ray binary*

The major argument in favour of a BH scenario is that the $L_{\rm R}/L_{\rm X}$ ratio is consistent with the scatter of the $L_{\rm R}$–$L_{\rm X}$ correlation for quiescent stellar mass BHs, from Gallo et al. (2014). The radio spectral index is not well constrained ($\alpha = -1.3^{+0.6}_{-0.7}$) but could be marginally consistent with the flat-to-inverted spectrum observed in quiescent systems (see e.g. Plotkin et al. 2019b), interpreted as self-absorbed synchrotron emission from a collimated jet. The low X-ray luminosity ($L_{\rm X}(1\text{–}10\ {\rm keV}) = 7.5^{+4.6}_{-3.5} \times 10^{29}$ erg s^{-1}; Table 2) is also consistent with a BH nature.

Although the fit quality is limited by the dearth of counts (27 counts between 0.5 and 10 keV), the (moderately) hard photon index ($\Gamma = 0.5 \pm 1.0$) of U97 could be a counterargument to this scenario. X-ray spectra of quiescent BHs are usually characterized by softer power laws ($\Gamma \sim 2.1$; Tomsick, Corbel & Kaaret 2001; Kong et al. 2002; Corbel, Tomsick & Kaaret 2006; Plotkin, Gallo & Jonker 2013; Reynolds et al. 2014). Conceivably, a quiescent BH, seen edge-on, would present a harder X-ray spectrum, as the X-rays could be heavily absorbed by part of the accretion disc.

Although the optical counterpart is not obviously blue (as might be expected in an accretion disc scenario), the quiescent nature of the disc at this time could permit the optical/UV light to be dominated by the companion star (e.g. in XTE J1118+480 and A0620−00; see Gallo et al. 2007).

[6] Although not published, D'Amico et al. have been timing PSR J1740−5340 at Parkes for a decade at 3 GHz, and their beam includes U18.

3.4.3 A white dwarf system?

As mentioned previously in Section 1.1, CVs are often observed to be radio sources, but they typically have rather low luminosities ($\lesssim 10^{25}$ erg s^{-1}) in the radio (e.g. Barrett et al. 2017). Two highly magnetic WDs are unusually bright in the radio: AE Aqr (Eracleous et al. 1991) and AR Sco (Marsh et al. 2016). Both lie quite near to U97 in the X-ray/radio luminosity diagram (Fig. 4). Note that neither is a standard, accreting CV; AE Aqr is largely in the propeller regime (Eracleous & Horne 1996), while AR Sco is not thought to be accreting, but to be the first known WD pulsar. The negative radio spectral index of U97 contrasts with the positive radio spectral index of AR Sco, while AE Aqr attains its maximum radio flux density only in short flares; we measure U97 to have the same radio flux densities (37 and 38 μJy, respectively, with noise of 5.5/6.8 μJy per beam, respectively) in the two halves of our observation. Both AR Sco and AE Aqr are also quite blue, especially in the ultraviolet. This appears not to be the case for U97, according to the HUGS photometry (Fig. 2).

3.5 U108, W127, W129, and W135

U108 is near an extended object on the optical images, which was interpreted as interacting galaxies by Cohn et al. (2010). We found a 7.7 σ radio source 0.57 arcsec ($1.2P_{\rm err}$) from the nominal X-ray position, slightly outside the 95 per cent error circle; however, the radio position agrees closely with the optical counterpart, suggesting that the radio and X-ray sources are probably associated with these galaxies (Fig. 3).

W127, W129, and W135 are also likely to be extragalactic sources. Arguments for their non-member nature include their large offsets from the cluster centre and, more importantly, their apparently high X-ray absorption (see below), common in AGNs from the obscuring torus. W129 has a relatively 'soft' photon index of $\Gamma = 2.7^{+1.4}_{-1.2}$ (Table 2), but this fit requires heavy absorption of $N_{\rm H} = 1.2^{+6.6}_{-4.7} \times 10^{23}$ cm^{-2} (see Fig. A2). In fact, we searched in the *Mikulski Archive for Space Telescopes* (MAST)[7] and found that the position of W129 is marginally covered by an *HST* WFC3/IR observation, where we visually identified that W129 is associated with an extended source, likely an early-type galaxy (Fig. 3). W127 is deficient of soft X-ray counts, so seems also to be affected by absorption (see Table A1). A power-law fit to W135 results in a very hard $\Gamma = -0.2^{+1.0}_{-1.2}$. A negative value in this case fits the soft part of the spectrum, since we fixed the $N_{\rm H}$ to the cluster value, which is too low to compensate for the dearth of soft photons. Moreover, searches for possible optical counterparts to either W127 or W135 in the *Gaia* DR2 data base did not reveal any objects up to twice the X-ray error radii (Appendix A), suggesting an extragalactic nature.

4 DISCUSSION

The identification of U18 as a hidden MSP via its steep-spectrum radio emission is extremely exciting. Its identification in the second-nearest GC (making U18 one of the three nearest MSPs in GCs known) suggests that a substantial population of similar systems may exist, with implications for our understanding of the evolution of X-ray binaries into MSPs.

Evidence from previous studies (see Section 1.2) suggests that more than one mechanism for pulsar eclipses operates, with several works showing that the pulsar signal is absorbed at low frequencies (<1 GHz), but may be scattered at high frequencies. Our current study is unique in indicating that two different eclipse mechanisms appear to be operating in two different MSPs at 5.5 GHz. U12 suffers absorption (dimming by at least a factor of 2.8) during its 5.5-GHz eclipse, while U18 has a similar radio flux as U12 but remains undetected as a radio pulsar. Our detection of the radio counterpart to U18 strongly indicates a scattering process is at work in this system. It is particularly odd that U12 and U18 would show different eclipse mechanisms, as the two systems are remarkably similar in their radio flux, their X-ray flux, and their companion properties (both are sub-subgiants, located a magnitude below the subgiant branch). All three HUGS CMDs show a greater red excess in U18 than U12 (Fig. 2). This may suggest that the NS in U18 is in a wider orbit, so that less mass has been stripped away from its companion, leaving it redder (Ivanova et al. 2017). How this could relate to different absorption mechanisms and properties is unclear.

As suggested by Tavani (1991), it may be possible to search for gamma-ray pulsations from U18 to confirm its nature. Blind gamma-ray pulsation searches are only effective for isolated MSPs (Clark et al. 2018), but the example of PSR J1311−3430 (Pletsch et al. 2012; Romani 2012) shows that gamma-ray pulsations can be uncovered if an optical orbital ephemeris for the counterpart is available. Indeed, the orbital solution for U18 has recently been uncovered by Pichardo Marcano et al. (in preparation), suggesting the feasibility of such a search.

5 CONCLUSIONS

Our studies of the *Chandra* and ATCA observations reveal radio continuum counterparts to seven X-ray sources including a known MSP (U12; PSR 1740−5340), a 'hidden' pulsar (U18) likely obscured by matter stripped from the companion, a BH candidate (U97), a previously identified extragalactic source (U108), and three new sources (W127, W129, and W135), of which two (W127 and W135) are likely to be extragalactic, while the other, W129, has a definite match with a galaxy. The similarities between U12 and U18 and the detection of a steep-spectrum radio counterpart to U18 indicate different eclipsing mechanisms in these two sources, and we suggest that scattering is likely to be the dominant mechanism at high radio frequencies.

ACKNOWLEDGEMENTS

COH was supported by NSERC Discovery Grant RGPIN-2016-04602 and a Discovery Accelerator Supplement. JS acknowledges support from NSF grant AST-1308124 and a Packard Fellowship. JCAM-J was the recipient of an Australian Research Council Future Fellowship (FT140101082), funded by the Australian government. LC acknowledges support from *Chandra* G06-17040X. This work was primarily based on observations obtained with *Chandra* and ATCA. *Chandra* data reduction and analyses made use of the software provided by the Chandra X-ray Center (CXC) in the application package CIAO. X-ray spectral analyses in this work made use of software packages provided by the High Energy Astrophysics Science Archive Research Center (HEASARC), which is a service of the Astrophysics Science Division at NASA/GSFC and the High Energy Astrophysics Division of the Smithsonian Astrophysical Observatory. The ATCA is part of the Australia Telescope National Facility that is funded by the Australian Government for operation as a National Facility managed by CSIRO. We also used data from the European Space Agency (ESA) mission *Gaia*

[7] http://archive.stsci.edu/

(https://www.cosmos.esa.int/gaia), processed by the *Gaia* Data Processing and Analysis Consortium (DPAC, https://www.cosmos.esa.int/web/gaia/dpac/consortium). Funding for the DPAC has been provided by national institutions, in particular the institutions participating in the *Gaia* Multilateral Agreement.

REFERENCES

Abada-Simon M., Lecacheux A., Bastian T. S., Bookbinder J. A., Dulk G. A., 1993, ApJ, 406, 692
Al Noori H. et al., 2018, ApJ, 861, 89
Anderson J. et al., 2008, AJ, 135, 2055
Archibald A. M. et al., 2009, Science, 324, 1411
Arnaud K. A., 1996, in Jacoby G. H., Barnes J., eds, ASP Conf. Ser. Vol. 101, Astronomical Data Analysis Software and Systems V. Astron. Soc. Pac., San Francisco, p. 17
Arons J., Tavani M., 1993, ApJ, 403, 249
Bahramian A., Heinke C. O., Degenaar N., Chomiuk L., Wijnands R., Strader J., Ho W. C. G., Pooley D., 2015, MNRAS, 452, 3475
Bahramian A. et al., 2017, MNRAS, 467, 2199
Bahramian A. et al., 2018, https://doi.org/10.5281/zenodo.1252036, (Accessed October 6, 2019)
Bailer-Jones C. A. L., Rybizki J., Fouesneau M., Mantelet G., Andrae R., 2018, AJ, 156, 58
Bailyn C. D., Grindlay J. E., Garcia M. R., 1990, ApJ, 357, L35
Barrett P. E., Dieck C., Beasley A. J., Singh K. P., Mason P. A., 2017, AJ, 154, 252
Bassa C. et al., 2004, ApJ, 609, 755
Bassa C. G., Pooley D., Verbunt F., Homer L., Anderson S. F., Lewin W. H. G., 2008, A&A, 488, 921
Bates S. D., Lorimer D. R., Verbiest J. P. W., 2013, MNRAS, 431, 1352
Belloni D., Giersz M., Rivera Sandoval L. E., Askar A., Ciecielåg P., 2019, MNRAS, 483, 315
Benz A. O., Fuerst E., Kiplinger A. L., 1983, Nature, 302, 45
Bogdanov S., Archibald A. M., Hessels J. W. T., Kaspi V. M., Lorimer D., McLaughlin M. A., Ransom S. M., Stairs I. H., 2011, ApJ, 742, 97
Bogdanov S., Esposito P., Crawford Fronefield I., Possenti A., McLaughlin M. A., Freire P., 2014, ApJ, 781, 6
Bogdanov S., Grindlay J. E., van den Berg M., 2005, ApJ, 630, 1029
Bogdanov S., van den Berg M., Heinke C. O., Cohn H. N., Lugger P. M., Grindlay J. E., 2010, ApJ, 709, 241
Bogdanov S. et al., 2018, ApJ, 856, 54
Broderick J. W. et al., 2016, MNRAS, 459, 2681
Camilo F., Lorimer D. R., Freire P., Lyne A. G., Manchester R. N., 2000, ApJ, 535, 975
Camilo F., Rasio F. A., 2005, in Rasio F. A., Stairs I. H., eds, ASP Conf. Ser. Vol. 328, Binary Radio Pulsars. Astron. Soc. Pac., San Francisco, p. 147
Cash W., 1979, ApJ, 228, 939
Chanmugam G., 1987, Ap&SS, 130, 53
Cheng Z., Li Z., Xu X., Li X., 2018, ApJ, 858, 33
Chomiuk L., Strader J., Maccarone T. J., Miller-Jones J. C. A., Heinke C., Noyola E., Seth A. C., Ransom S., 2013, ApJ, 777, 69
Chugainov P. F., 1966, Inf. Bull. Var. Stars, 122, 1
Clark C. J. et al., 2018, Sci. Adv., 4, eaao7228
Cohn H. N. et al., 2010, ApJ, 722, 20
Colpi M., Possenti A., Gualandris A., 2002, ApJ, 570, L85
Coppejans D. L., Körding E. G., Miller-Jones J. C. A., Rupen M. P., Knigge C., Sivakoff G. R., Groot P. J., 2015, MNRAS, 451, 3801
Coppejans R. et al., 2016, MNRAS, 463, 3260
Corbel S., Coriat M., Brocksopp C., Tzioumis A. K., Fender R. P., Tomsick J. A., Buxton M. M., Bailyn C. D., 2013, MNRAS, 428, 2500
Corbel S., Tomsick J. A., Kaaret P., 2006, ApJ, 636, 971
Davies M. B., 1997, MNRAS, 288, 117
Deller A. T. et al., 2015, ApJ, 809, 13
de Martino D. et al., 2015, MNRAS, 454, 2190
Dempsey R. C., Linsky J. L., Fleming T. A., Schmitt J. H. M. M., 1993, ApJS, 86, 599
Drake S. A., Simon T., Linsky J. L., 1989, ApJS, 71, 905
D'Amico N., Lyne A. G., Manchester R. N., Possenti A., Camilo F., 2001a, ApJ, 548, L171
D'Amico N., Possenti A., Manchester R. N., Sarkissian J., Lyne A. G., Camilo F., 2001b, ApJ, 561, L89
Eracleous M., Halpern J., Patterson J., 1991, ApJ, 382, 290
Eracleous M., Horne K., 1996, ApJ, 471, 427
Fabian A. C., Pringle J. E., Rees M. J., 1975, MNRAS, 172, 15p
Feldman P. A., 1983, in Byrne P. B., Rodono M., eds, Astrophysics and Space Science Library, Vol. 102, Activity in Red-Dwarf Stars. Reidel, Dordrecht, p. 429
Ferraro F. R., Possenti A., D'Amico N., Sabbi E., 2001, ApJ, 561, L93
Ferraro F. R., Sabbi E., Gratton R., Possenti A., D'Amico N., Bragaglia A., Camilo F., 2003, ApJ, 584, L13
Forestell L. M., Heinke C. O., Cohn H. N., Lugger P. M., Sivakoff G. R., Bogdanov S., Cool A. M., Anderson J., 2014, MNRAS, 441, 757
Freire P. C. C., 2005, in Rasio F. A., Stairs I. H., eds, ASP Conf. Ser. Vol. 328, Binary Radio Pulsars. Astron. Soc. Pac., San Francisco, p. 405
Fruchter A. S., Goss W. M., 1992, ApJ, 384, L47
Fruchter A. S., Stinebring D. R., Taylor J. H., 1988, Nature, 333, 237
Fruscione A. et al., 2006, in Silva D. R., Doxsey R. E., eds, Proc. SPIE Conf. Ser. Vol. 6270, Observatory Operations: Strategies, Processes, and Systems. SPIE, Bellingham, p. 62701V
Gaia Collaboration, 2016, A&A, 595, A1
Gaia Collaboration, 2018a, A&A, 616, A1
Gaia Collaboration, 2018b, A&A, 616, A12
Gallo E., Degenaar N., van den Eijnden J., 2018, MNRAS, 478, L132
Gallo E., Migliari S., Markoff S., Tomsick J. A., Bailyn C. D., Berta S., Fender R., Miller-Jones J. C. A., 2007, ApJ, 670, 600
Gallo E., Miller B. P., Fender R., 2012, MNRAS, 423, 590
Gallo E. et al., 2014, MNRAS, 445, 290
García-Sánchez J., Paredes J. M., Ribó M., 2003, A&A, 403, 613
Gehrels N., 1986, ApJ, 303, 336
Grindlay J. E., Heinke C., Edmonds P. D., Murray S. S., 2001a, Science, 292, 2290
Grindlay J. E., Heinke C. O., Edmonds P. D., Murray S. S., Cool A. M., 2001b, ApJ, 563, L53
Grindlay J. E., Hertz P., Steiner J. E., Murray S. S., Lightman A. P., 1984, ApJ, 282, L13
Gudel M., 1992, A&A, 264, L31
Guedel M., Benz A. O., 1993, ApJ, 405, L63
Guillot S., Rutledge R. E., Brown E. F., 2011, ApJ, 732, 88
Gusinskaia N. V. et al., 2020, MNRAS, 492, 2858
Haggard D., Cool A. M., Davies M. B., 2009, ApJ, 697, 224
Harding A. K., Gaisser T. K., 1990, ApJ, 358, 561
Harris W. E., 1996, AJ, 112, 1487
Heinke C. O., Grindlay J. E., Lugger P. M., Cohn H. N., Edmonds P. D., Lloyd D. A., Cool A. M., 2003, ApJ, 598, 501
Heinke C. O. et al., 2014, MNRAS, 444, 443
Hill A. B. et al., 2011, MNRAS, 415, 235
Hills J. G., 1976, MNRAS, 175, 1P
Hjellming R. M., Gibson D. M., 1980, in Kundu M. R., Gergely T. E., eds, Proc. IAU Symp. 86, Radio Physics of the Sun. Reidel, Dordrecht, p. 209
Hong J., van den Berg M., Schlegel E. M., Grindlay J. E., Koenig X., Laycock S., Zhao P., 2005, ApJ, 635, 907
Huang R. H. H., Kong A. K. H., Takata J., Hui C. Y., Lin L. C. C., Cheng K. S., 2012, ApJ, 760, 92
Hui C. Y., Tam P. H. T., Takata J., Kong A. K. H., Cheng K. S., Wu J. H. K., Lin L. C. C., Wu E. M. H., 2014, ApJ, 781, L21
Hui C. Y. et al., 2015, ApJ, 801, L27
Ivanova N., da Rocha C. A., Van K. X., Nandez J. L. A., 2017, ApJ, 843, L30
Ivanova N., Heinke C. O., Rasio F. A., Taam R. E., Belczynski K., Fregeau J., 2006, MNRAS, 372, 1043
Kaluzny J., Rucinski S. M., Thompson I. B., 2003, AJ, 125, 1546
Kong A. K. H., Bassa C., Pooley D., Lewin W. H. G., Homer L., Verbunt F., Anderson S. F., Margon B., 2006, ApJ, 647, 1065

Kong A. K. H., McClintock J. E., Garcia M. R., Murray S. S., Barret D., 2002, ApJ, 570, 277
Kundu M. R., Shevgaonkar R. K., 1985, ApJ, 297, 644
Kurbatov E. P., Zhilkin A. G., Bisikalo D. V., 2019, Astron. Rep., 63, 25
Körding E., Rupen M., Knigge C., Fender R., Dhawan V., Templeton M., Muxlow T., 2008, Science, 320, 1318
Leiner E., Mathieu R. D., Geller A. M., 2017, ApJ, 840, 67
Lewin W. H. G., Joss P. C., 1983, in Lewin W. H. G., van den Heuvel E. P. J., eds, Accretion-Driven Stellar X-Ray Sources. Cambridge Univ. Press, Cambridge, p. 41
Li D., Lin F. X., Main R., Pen U.-L., van Kerkwijk M. H., Yang I.-S., 2019, MNRAS, 484, 5723
Lorimer D. R., Yates J. A., Lyne A. G., Gould D. M., 1995, MNRAS, 273, 411
Ludlam R., Miller J. M., Miller-Jones J., Reynolds M., 2017, Astron. Telegram, 10690, 1
Lyne A. G. et al., 1990, Nature, 347, 650
Manchester R. N., 2017, JA&A, 38, 42
Marsh T. R. et al., 2016, Nature, 537, 374
Mason P. A., Gray C. L., 2007, ApJ, 660, 662
McMullin J. P., Waters B., Schiebel D., Young W., Golap K., 2007, in Shaw R. A., Hill F., Bell D. J., eds, ASP Conf. Ser. Vol. 376, Astronomical Data Analysis Software and Systems XVI. Astron. Soc. Pac., San Francisco, p. 127
Meintjes P. J., Venter L. A., 2005, MNRAS, 360, 573
Migliari S., Fender R. P., 2006, MNRAS, 366, 79
Miller-Jones J. C. A., Jonker P. G., Maccarone T. J., Nelemans G., Calvelo D. E., 2011, ApJ, 739, L18
Miller-Jones J. C. A., Sivakoff G. R., Knigge C., Körding E. G., Templeton M., Waagen E. O., 2013, Science, 340, 950
Miller-Jones J. C. A. et al., 2015, MNRAS, 453, 3918
Mooley K. P. et al., 2017, MNRAS, 467, L31
Mucciarelli A., Salaris M., Lanzoni B., Pallanca C., Dalessandro E., Ferraro F. R., 2013, ApJ, 772, L27
Nardiello D. et al., 2018, MNRAS, 481, 3382
Orosz J. A., van Kerkwijk M. H., 2003, A&A, 397, 237
Osten R. A., Brown A., Ayres T. R., Linsky J. L., Drake S. A., Gagné M., Stern R. A., 2000, ApJ, 544, 953
Papitto A. et al., 2013, Nature, 501, 517
Pecaut M. J., Mamajek E. E., 2013, ApJS, 208, 9
Piotto G. et al., 2015, AJ, 149, 91
Pletsch H. J. et al., 2012, Science, 338, 1314
Plotkin R. M., Gallo E., Jonker P. G., 2013, ApJ, 773, 59
Plotkin R. M., Miller-Jones J. C. A., Chomiuk L., Strader J., Bruzewski S., Bundas A., Smith K. R., Ruan J. J., 2019a, ApJ, 874, 13
Plotkin R. M., Miller-Jones J. C. A., Chomiuk L., Strader J., Bruzewski S., Bundas A., Smith K. R., Ruan J. J., 2019b, ApJ, 874, 13
Plotkin R. M. et al., 2017, ApJ, 834, 104
Polzin E. J., Breton R. P., Bhattacharyya B., Scholte D., Sobey C., Stappers B. W., 2020, preprint, (arXiv:1908.04778)
Polzin E. J., Breton R. P., Stappers B. W., Bhattacharyya B., Janssen G. H., Osłowski S., Roberts M. S. E., Sobey C., 2019, MNRAS, 490, 889
Polzin E. J. et al., 2018, MNRAS, 476, 1968
Pooley D., Hut P., 2006, ApJ, 646, L143
Pooley D. et al., 2003, ApJ, 591, L131
Ratti E. M. et al., 2012, MNRAS, 423, 2656
Reynolds M. T., Reis R. C., Miller J. M., Cackett E. M., Degenaar N., 2014, MNRAS, 441, 3656
Ridolfi A. et al., 2016, MNRAS, 462, 2918
Rivera Sandoval L. E. et al., 2018, MNRAS, 475, 4841
Roberts M. S. E., 2013, in van Leeuwen J., ed., Proc. IAU Symp. 291, Neutron Stars and Pulsars: Challenges and Opportunities After 80 Years. Cambridge Univ. Press, Cambridge, p. 127
Romani R. W., 2012, ApJ, 754, L25
Romani R. W., Sanchez N., 2016, ApJ, 828, 7
Romani R. W., Shaw M. S., 2011, ApJ, 743, L26
Roy J. et al., 2015, ApJ, 800, L12
Rushton A. P. et al., 2016, MNRAS, 463, 628
Russell T. D. et al., 2016, MNRAS, 460, 3720
Sabbi E., Gratton R., Ferraro F. R., Bragaglia A., Possenti A., D'Amico N., Camilo F., 2003, ApJ, 589, L41
Sarajedini A. et al., 2007, AJ, 133, 1658
Sault R. J., Teuben P. J., Wright M. C. H., 1995, in Shaw R. A., Payne H. E., Hayes J. J. E., eds, ASP Conf. Ser. Vol. 77, Astronomical Data Analysis Software and Systems IV. Astron. Soc. Pac., San Francisco, p. 433
Shishkovsky L. et al., 2018, ApJ, 855, 55
Sieber W., 1973, A&A, 28, 237
Soleri P. et al., 2010, MNRAS, 406, 1471
Stappers B. W., Bailes M., Lyne A. G., Camilo F., Manchester R. N., Sandhu J. S., Toscano M., Bell J. F., 2001, MNRAS, 321, 576
Stovall K. et al., 2014, ApJ, 791, 67
Strader J., Chomiuk L., Maccarone T. J., Miller-Jones J. C. A., Seth A. C., 2012, Nature, 490, 71
Strader J. et al., 2019, ApJ, 872, 42
Tavani M., 1991, ApJ, 379, L69
Tetarenko B. E. et al., 2016, ApJ, 825, 10
Thompson C., Blandford R. D., Evans C. R., Phinney E. S., 1994, ApJ, 422, 304
Tomsick J. A., Corbel S., Kaaret P., 2001, ApJ, 563, 229
Tremou E. et al., 2018, ApJ, 862, 16
Tudor V. et al., 2017, MNRAS, 470, 324
van Staden A. D., Antoniadis J., 2016, ApJ, 833, L12
Verbunt F., Meylan G., 1988, A&A, 203, 297
Wadiasingh Z., Harding A. K., Venter C., Böttcher M., Baring M. G., 2017, ApJ, 839, 80
Wadiasingh Z., Venter C., Harding A. K., Böttcher M., Kilian P., 2018, ApJ, 869, 120
Wilms J., Allen A., McCray R., 2000, ApJ, 542, 914
Wynn G. A., King A. R., Horne K., 1997, MNRAS, 286, 436

APPENDIX A: AN UPDATED X-RAY SOURCE CATALOGUE AND TENTATIVE IDENTIFICATION OF NEW SOURCES

Our X-ray catalogue (Table A1) includes sources within the 2.9 arcmin half-light radius ($r_{\rm h}$, as updated by Harris 1996, 2010 revision; note that Bogdanov et al. 2010 used a previous Harris catalogue version with $r_{\rm h} = 2.33$ arcmin to search for sources) and source positions with updated astrometry from *Gaia* DR2. We adopt source counts from Bogdanov et al. (2010) and calculate counts in the same bands using the CIAO `srcflux` tool, for the new sources (Section 2.2). Most of these sources are outside the *HST* field of view, so direct photometric identification might be hard. However, tenuous classification is still possible solely based on the X-ray hardness. For this purpose, we define an X-ray hardness ratio

$$X_{\rm C} \equiv 2.5 \log_{10} \left(\frac{C_{0.5-1.5\,\rm keV}}{C_{1.5-6\,\rm keV}} \right), \tag{A1}$$

where $C_{0.5-1.5\,\rm keV}$ and $C_{1.5-6\,\rm keV}$ are X-ray counts in 0.5–1.5 and 1.5–6 keV, respectively. The distribution of $X_{\rm C}$ is shown in Fig. A1, which plots 0.5–6 keV fluxes versus $X_{\rm C}$ for known and new sources.

In principle, most of the very hard ($X_{\rm C} \lesssim 0$) sources that lack soft counts are very likely background sources (e.g. AGNs) with high values of $N_{\rm H}$. These include W127, W129, W135, W141, and W142. A typical example is W129, which is heavily absorbed and has zero counts in the 0.5–1.5 keV band. The best-fitting power-law model (Fig. A2) suggests an $N_{\rm H} = 11.8^{+6.6}_{-4.7} \times 10^{22}\,{\rm cm}^{-2}$, which is clearly above the cluster value of $N_{\rm H} = 1.57 \times 10^{21}\,{\rm cm}^{-2}$. Moreover, clear detections in the radio bands (Section 3.5) further corroborate their AGN nature.

The soft sources ($X_{\rm C} \gtrsim 1.8$), including W126, W132, W136, W139, W143, W144, W145, and W146, are likely faint ABs or CVs, whose spectra can be fairly reproduced by either a blackbody

Table A1. X-ray catalogue of source within the 2.9 arcmin half-light radius.

ID	RA	Dec.	$P_{\rm err}^{a}$	Counts[a]		Flux[b]
	(J2000)			0.5–1.5 keV	1.5–6 keV	0.5–6.0 keV
U5	17:40:54.539	−53:40:44.912	0.33	167	31	41.7
U7	17:40:52.843	−53:41:22.170	0.32	252	150	84.6
U10	17:40:48.987	−53:39:48.986	0.29	283	1504	390.8
U11	17:40:45.786	−53:40:41.898	0.32	72	55	26.7
U12	17:40:44.627	−53:40:41.957	0.30	382	363	157.3
U13	17:40:44.093	−53:40:39.506	0.31	107	135	51.4
U14	17:40:43.340	−53:41:55.821	0.40	17	10	5.7
U15	17:40:42.923	−53:40:34.127	0.34	42	9	11.2
U16	17:40:42.659	−53:42:15.698	0.42	15	10	5.4
U17	17:40:42.659	−53:40:19.628	0.28	5358	6114	2458.0
U18	17:40:42.619	−53:40:27.964	0.29	995	1142	470.2
U19	17:40:42.317	−53:40:29.073	0.28	2777	5934	1927.3
U21	17:40:41.843	−53:40:21.740	0.29	1974	2279	901.4
U22	17:40:41.711	−53:40:29.380	0.31	104	131	50.3
U23	17:40:41.605	−53:40:19.624	0.28	1677	5915	1609.5
U24	17:40:41.481	−53:40:04.790	0.28	4797	353	1088.8
U25	17:40:41.248	−53:40:26.164	0.33	39	49	18.7
U28	17:40:38.915	−53:39:51.472	0.30	351	629	206.1
U31	17:40:34.213	−53:41:15.588	0.37	26	18	9.5
U41	17:40:45.015	−53:39:55.544	0.36	31	4	7.5
U42	17:40:43.064	−53:38:31.633	0.34	141	15	33.0
U43	17:40:40.556	−53:40:23.180	0.36	25	10	7.4
U60	17:40:47.825	−53:41:28.649	0.41	10	11	4.4
U61	17:40:45.231	−53:40:28.964	0.32	79	85	34.8
U62	17:40:30.426	−53:39:17.921	0.48	12	5	3.7
U63	17:40:31.680	−53:38:46.731	0.42	31	7	8.0
U65	17:40:37.578	−53:39:18.215	0.43	14	3	3.6
U66	17:40:38.952	−53:38:49.981	0.48	9	4	2.7
U67	17:40:40.074	−53:40:16.880	0.41	8	6	3.0
U68	17:40:40.694	−53:38:33.180	0.44	1	20	4.4
U69	17:40:40.880	−53:40:17.513	0.37	15	9	5.1
U70	17:40:41.705	−53:40:33.608	0.32	59	41	22.1
U73	17:40:42.692	−53:39:29.145	0.38	22	8	6.3
U75	17:40:43.662	−53:40:30.993	0.39	9	10	4.2
U76	17:40:43.827	−53:41:16.679	0.38	21	7	5.9
U77	17:40:44.140	−53:42:11.808	0.42	18	7	5.2
U79	17:40:46.415	−53:40:04.248	0.38	18	9	5.9
U80	17:40:46.445	−53:41:56.863	0.39	20	15	7.4
U81	17:40:46.482	−53:41:15.771	0.38	15	11	5.5
U82	17:40:48.549	−53:39:39.775	0.37	31	9	8.6
U83	17:40:49.636	−53:40:43.350	0.46	5	6	2.4
U84	17:40:54.815	−53:40:20.169	0.40	32	5	7.8
U86	17:40:37.483	−53:41:47.651	0.35	56	11	14.6
U87	17:40:42.888	−53:40:26.772	0.37	14	10	5.3
U88	17:40:42.848	−53:40:23.886	0.37	20	8	6.2
U89	17:40:43.651	−53:40:24.927	0.41	11	3	3.1
U90	17:40:41.808	−53:40:14.924	0.36	26	8	7.2
U91	17:40:42.422	−53:40:42.510	0.40	6	9	3.3
U92	17:40:43.923	−53:40:35.690	0.40	11	4	3.2
U93	17:40:42.361	−53:40:47.315	0.42	6	7	2.8
U94	17:40:42.893	−53:40:49.413	0.40	14	2	3.4
U95	17:40:40.334	−53:40:44.916	0.47	4	4	1.7
U96	17:40:39.090	−53:40:23.414	0.42	11	2	2.7
U97	17:40:43.916	−53:40:05.702	0.44	4	6	2.2
U98	17:40:41.006	−53:40:58.883	0.41	12	2	3.0
U99	17:40:46.439	−53:40:30.767	0.50	6	1	1.5
U100	17:40:38.212	−53:40:46.872	0.45	6	4	2.1
U101	17:40:45.412	−53:41:01.797	0.39	19	3	4.6
U102	17:40:38.877	−53:39:43.446	0.40	11	9	4.2
U103	17:40:35.718	−53:40:13.018	0.44	9	3	2.5
U104	17:40:43.138	−53:39:29.280	0.44	5	8	2.8

Table A1 – *continued*

ID	RA	Dec.	$P_{\rm err}^{a}$	Counts[a]		Flux[b]
	(J2000)			0.5–1.5 keV	1.5–6 keV	0.5–6.0 keV
U105	17:40:36.535	−53:41:08.319	0.44	8	5	2.7
U106	17:40:43.768	−53:39:17.814	0.51	3	5	1.7
U107	17:40:34.119	−53:40:17.295	0.39	16	10	5.4
U108	17:40:52.105	−53:39:48.404	0.46	9	6	3.2
U109	17:40:52.755	−53:40:53.217	0.50	8	3	2.3
U110	17:40:33.455	−53:39:17.335	0.50	8	3	2.6
U111	17:40:29.884	−53:40:27.207	0.45	3	14	3.7
U112	17:40:50.385	−53:39:06.322	0.53	7	3	2.1
U113	17:40:42.764	−53:40:21.041	0.31	161	61	50.0
U114	17:40:43.480	−53:40:34.662	0.45	4	5	2.0
U116	17:40:42.247	−53:40:20.292	0.36	15	14	6.3
U117	17:40:42.164	−53:40:25.882	0.41	7	6	2.9
U118	17:40:41.587	−53:40:16.202	0.43	3	8	2.3
U119	17:40:41.272	−53:40:19.672	0.40	4	11	3.2
U120	17:40:46.528	−53:40:15.962	0.53	6	0	1.3
U121	17:40:33.642	−53:39:35.282	0.50	2	8	2.1
U122	17:40:47.914	−53:39:25.152	0.58	1	5	1.3
U123	17:40:49.632	−53:38:46.252	0.60	2	6	1.7
W124	17:40:30.511	−53:42:34.201	0.38	103	108	49.1
W125	17:40:27.976	−53:42:00.059	0.39	73	66	30.6
W126	17:40:59.672	−53:40:39.095	0.38	54	10	8.1
W127	17:40:58.559	−53:40:14.878	0.52	3	10	3.0
W128	17:40:56.736	−53:39:39.863	0.33	102	104	45.5
W129	17:40:56.204	−53:39:11.229	0.35	0	123	61.6
W130	17:40:50.597	−53:38:25.760	0.34	103	90	36.6
W131	17:40:37.690	−53:42:46.340	0.42	32	22	9.4
W132	17:40:36.503	−53:42:41.158	0.52	24	1	4.5
W133	17:40:58.337	−53:41:53.413	0.37	78	40	23.3
W134	17:40:42.036	−53:40:37.877	0.41	9	5	2.9
W135	17:40:48.754	−53:43:04.444	0.64	2	9	5.4
W136	17:40:53.157	−53:40:58.363	0.63	5	0	0.6
W137	17:40:58.548	−53:39:17.142	0.42	42	31	14.8
W138	17:40:50.710	−53:43:02.721	0.73	5	5	3.0
W139	17:40:29.296	−53:42:21.018	0.85	17	5	4.1
W140	17:40:53.868	−53:41:30.826	0.57	4	6	1.8
W141	17:40:26.669	−53:41:18.152	0.74	1	16	8.8
W142	17:41:00.896	−53:40:52.215	0.62	2	12	4.2
W143	17:40:22.994	−53:40:34.913	0.72	17	4	3.6
W144	17:40:33.992	−53:39:07.244	0.74	8	2	2.3
W145	17:40:27.889	−53:38:45.537	0.88	22	8	5.6
W146	17:40:57.386	−53:38:40.507	0.65	23	0	2.8

[a] $P_{\rm err}$ (in arcsec) and counts for U-sources are from Bogdanov et al. (2010). Counts of the W sources are calculated by `srcflux`.
[b] Source fluxes are in units of 10^{-16} erg s^{-1} cm^{-2}; fluxes for all U sources are from Bogdanov et al. (2010), while fluxes for the W sources are model-independent fluxes calculated by `srcflux`.

with $kT_{\rm bb}$ between 0.1 and 0.3 keV or a thermal plasma model (e.g. `vmekal` in XSPEC) with typical plasma temperature $\lesssim$2 keV. Blackbody fits give $kT_{\rm bb}$ and $R_{\rm bb}$ similar to those of MSPs, which seems reasonable since MSPs far from the cluster centre have been observed in other core-collapsed GCs (see e.g. Colpi, Possenti & Gualandris 2002; Forestell et al. 2014); however, we found the spectra are more likely reproduced by optically thin low-temperature plasma, as they possess evidence of emission features at low energies (e.g. emission line at ∼0.8–1 keV that overlaps the Fe L-shell emission), which is more common among faint ABs or CVs. As an example, we show the spectrum of W145 fitted with a `vmekal` model in Fig. A2, with a clear emission feature at ∼1 keV.

Finally, sources with somewhat more balanced spectra, including W124, W125, W128, W130, W131, W133, W134, W137, W138, and W140, could be either background AGNs or faint CVs.

We tried to search for optical counterparts with searching radii up to $2P_{\rm err}$ for these new sources, using the *Gaia* DR2 archive (Gaia Collaboration 2016, 2018a). Limited by the low stellar density at the cluster outskirt, detecting multiple objects in the sub-arcsecond error circles might be rare. Indeed, in all searching radii, we found at most one *Gaia* source (Table A2); however, these unique objects are not necessarily real counterparts, as fainter objects within the searching radii might have magnitudes above the *Gaia* limit (*G*-band limiting magnitude ≈21). Nevertheless, non-detections might still indicate a distant nature for the source. In fact, all of the heavily absorbed sources mentioned earlier have empty searching regions, which further supports their nature as distant objects.

As complementary information, we check the photometric colours of these potential counterparts using the *Gaia* two-band

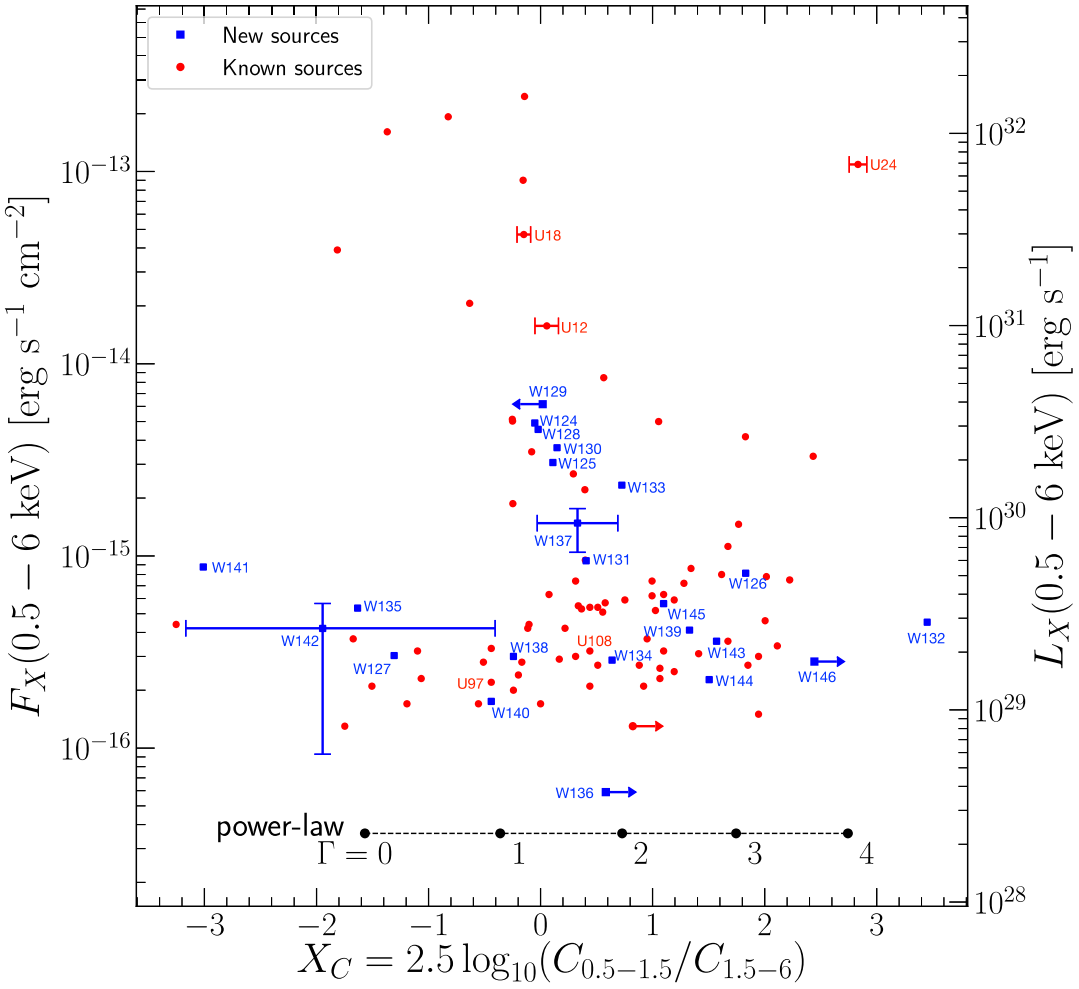

Figure A1. X-ray CMD plotting 0.5–6 keV fluxes (left scale) and luminosities (right scale at the cluster distance) versus hardness ratios (X_C, defined in eq. A1) for known (red circles) and new (blue squares) sources. X_C values and fluxes of the known sources are adapted from Bogdanov et al. (2010), while were calculated by `srcflux` (Section 2.2) for the new sources. For better readability, we only labelled the relevant known sources and the new sources, and put error bars on several sources to represent uncertainties at different flux levels. Upper/lower limits and errors in X_C are at the 90 per cent confidence as derived according to methods in Gehrels (1986). We also indicate the locations of power-law models with different photon indices (Γ).

(G_{BP} and G_{RP}) magnitudes. We show a *Gaia* $G_{BP} - G_{RP}$ CMD in Fig. A4 using stars within a 3 arcmin circular region centred on the cluster. We also make use of PM information from the *Gaia* data base to confirm membership, only accepting sources that have PMs consistent with the cluster systematic PM ($\mu_\alpha = 3.2908 \pm 0.0026$ mas yr^{-1}, $\mu_\delta = -17.5908 \pm 0.0025$ mas yr^{-1}; see Gaia Collaboration 2018b) at 5 σ level as cluster members.

There are five sources, W132, W133, W138, W143, and W146, that have clearly inconsistent PMs with the cluster. The red excesses in W132 and W143 (Fig. A4) are consistent with their foreground nature (as suggested by their distances in Table A2), while the counterparts to W133 and W146 appear to be bright stars with blue excesses. W132 has a more definite binarity with a *Gaia*-measured radial velocity of $|v_r| = 10.11 \pm 1.97$ km s^{-1}. W133 has a PM clearly discordant with the cluster (Fig. A3). Intriguingly, W133 is a background source, but the counterpart distance is just a few hundred parsecs greater than the cluster (Table A2). We suspect that W133 is either a halo object or a 'runaway' close binary – likely a CV – ejected by dynamical encounters in the core. The stars found near W138 and W146 could be chance coincidences, as they are relatively far from the X-ray positions.

Three stars in the list are found to have PMs consistent with the cluster value. The PM-selected cluster member W136 has a red giant counterpart, so it could be an RS CVn system. W139 has a definite association with the cluster, but is so faint that no further photometric information is available. W145 has a counterpart consistent with the MS, but is likely to be a chance coincidence, as it lies at $\sim 2P_{err}$ off the X-ray position.

Finally, W134 is within the *HST* field of view, so HUGS photometry is available. We found three stars (Fig. A5) with colours consistent with the MS in the UV_{275}–U_{336} and U_{336}–B_{438} CMDs, while in the V_{606}–I_{814} CMD, there is one star (W134-2) that exhibits a very mild red excess relative to the MS (Fig. 2), which we think is more likely to be the counterpart. W134-2 has a definite cluster membership probability of 98.3 per cent but is less likely a chance coincidence compared to the other two.

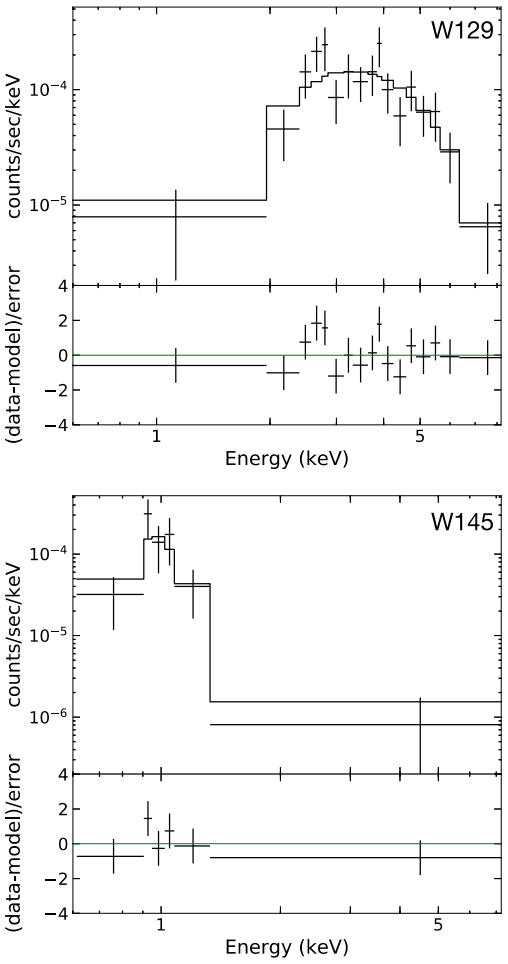

Figure A2. *Chandra* ACIS-S spectra of W129 (top) and W145 (bottom) overplotted with best-fitting power-law (W129) and `vmekal` (W145) model. The bottom panel of each plot shows the fitting residuals. The spectra are rebinned only for plotting purpose.

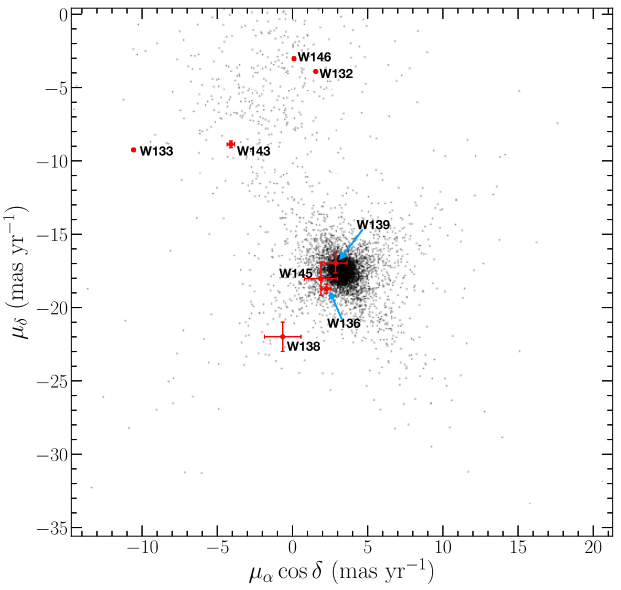

Figure A3. PMs from *Gaia* DR2 of stars within a 3 arcmin searching radius. The plot is centred on the cluster PM at $\mu_\alpha = 3.2908 \pm 0.0026$ mas yr^{-1} and $\mu_\delta = -17.5908 \pm 0.0025$ mas yr^{-1}. PM of each counterpart is indicated with red dot and 1 σ error bars.

Table A2. Optical counterparts to the new sources.

ID	Optical position RA	Dec.	Offset[a] (arcsec; $P_{\rm err}$)	Magnitudes[b] $G_{\rm BP}$	$G_{\rm RP}$	Membership[c]	Distance[d] (kpc)	Comments
W126	17:40:59.662	−53:40:39.001	0.13; 0.34	–	–	–	–	Faint AB or CV?
W131	17:40:37.686	−53:42:46.324	0.04; 0.10	–	–	–	–	Faint AB or CV?
W132	17:40:36.481	−53:42:41.151	0.20; 0.38	14.21	12.76	Foreground	$0.257^{+0.002}_{-0.002}$	Foreground AB?
W133	17:40:58.332	−53:41:53.318	0.11; 0.29	14.69	14.15	Background	$2.84^{+0.31}_{-0.26}$	Background CV?
W134	17:40:42.024	−53:40:37.854	0.11; 0.27	20.30	19.10	Member	$1.82^{+0.38}_{-0.27}$	Faint AB or CV?
W136	17:40:53.174	−53:40:58.642	0.32; 0.51	15.02	13.97	Member	$1.57^{+0.72}_{-0.38}$	RS CVn?
W138	17:40:50.856	−53:43:03.335	1.43; 1.96	–	–	Foreground	$0.58^{+0.76}_{-0.21}$	–
W139	17:40:29.293	−53:42:21.196	0.18; 0.21	–	–	Member	$3.59^{+3.32}_{-1.79}$	Faint AB or CV?
W143	17:40:22.925	−53:40:34.066	1.04; 1.45	17.07	15.89	Foreground	$1.36^{+0.40}_{-0.30}$	Foreground AB?
W144	17:40:33.890	−53:39:08.198	1.32; 1.78	16.86	15.92	–	–	–
W145	17:40:27.722	−53:38:45.047	1.56; 1.78	19.23	18.26	Member	$3.13^{+3.30}_{-1.83}$	Faint AB or CV?
W146	17:40:57.314	−53:38:39.885	0.89; 1.37	13.17	12.42	Foreground	$0.70^{+0.02}_{-0.02}$	Faint AB or CV?

[a]Offsets from the X-ray positions in terms of arcsec and $P_{\rm err}$.
[b]Magnitudes in the *Gaia* $G_{\rm BP}$ and $G_{\rm RP}$ bandpasses; for W134, the first and second columns correspond to magnitudes at the *HST*/ACS F606W and F814W filters, respectively.
[c]Cluster membership determinations based on *Gaia* PMs and/or distances or, for W134, the membership probability from the HUGS data.
[d]Distance estimates according to Bailer-Jones et al. (2018). The reported errors are at the 68 per cent confidence level

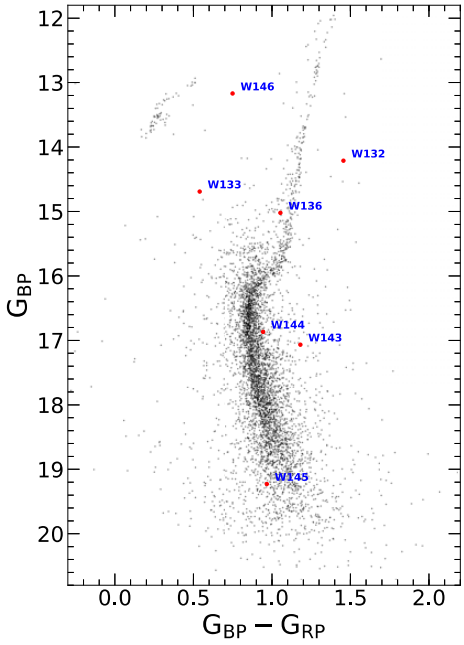

Figure A4. Gaia CMD plotting $G_{BP} - G_{RP}$ colours versus G_{BP} band magnitudes. The counterparts are indicated with red filled circles.

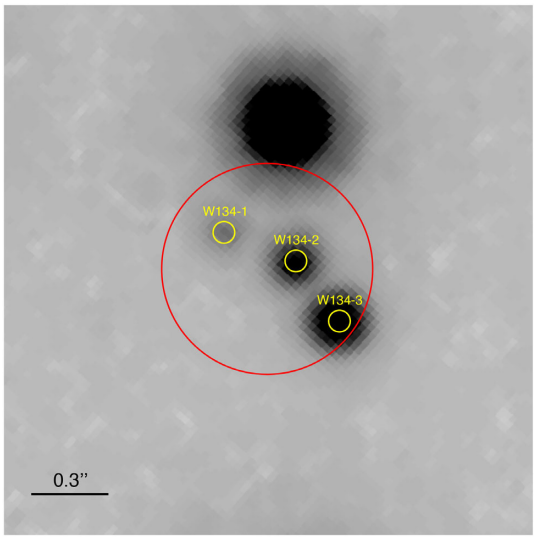

Figure A5. *HST*/ACS R625W finding chart for W134 showing a 2.1 arcsec × 2.1 arcsec region centred on the nominal X-ray position of W134. North is up and east is to the left. The red circle indicates the *Chandra* 95 per cent error region, while likely counterparts are indicated with yellow circles.

This paper has been typeset from a TEX/LATEX file prepared by the author.